iScience

Article

β-adrenergic signaling modulates breast cancer cell mechanical behaviors through a RhoA-ROCK-myosin II axis

Graphical abstract

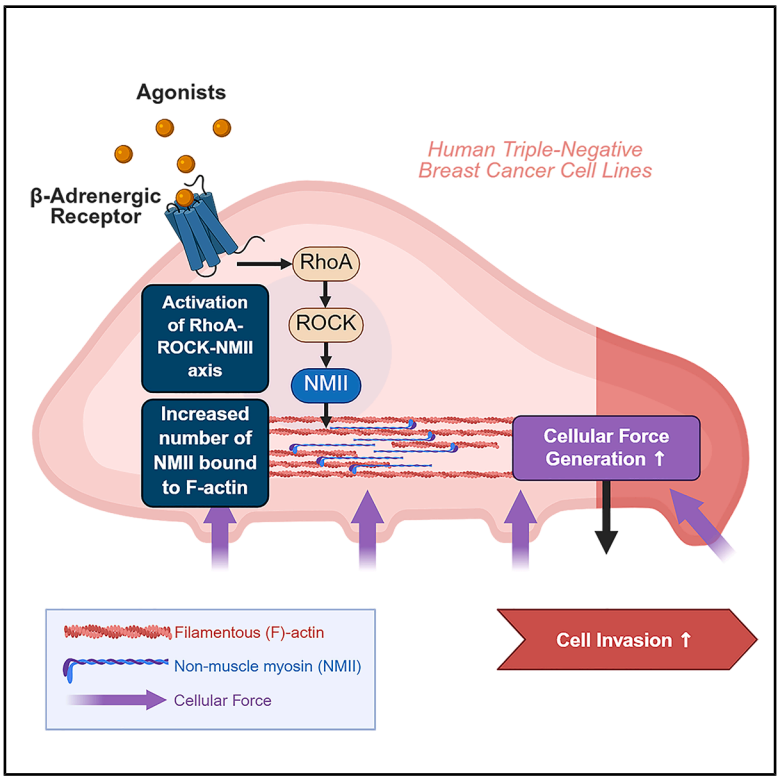

Highlights

- Activation of βAR signaling increases the force generation of breast cancer cells
- βAR activation increases the number of myosin II motors bound to actin
- We identified a βAR-RhoA-ROCK-NMII axis in breast cancer cells
- A βAR-RhoA-ROCK-NMII axis regulates the motility of breast cancer cells

Authors

Tae-Hyung Kim, Minh-Tam Tran Le, Mijung Oh, ..., Erica K. Sloan, Parag Katira, Amy C. Rowat

Correspondence

takim@salud.unm.edu (T.-H.K.), rowat@ucla.edu (A.C.R.)

In brief

Mechanobiology; Cell biology; Functional aspects of cell biology

Kim et al., 2025, iScience *28*, 112676
June 20, 2025 © 2025 The Author(s). Published by Elsevier Inc.
https://doi.org/10.1016/j.isci.2025.112676

CellPress

iScience

CellPress
OPEN ACCESS

Article

β-adrenergic signaling modulates breast cancer cell mechanical behaviors through a RhoA-ROCK-myosin II axis

Tae-Hyung Kim,[1,13,15,*] Minh-Tam Tran Le,[2] Mijung Oh,[13] Esteban Vazquez-Hidalgo,[10,11] Bryanna Chavez,[1] Donald M. Lamkin,[4] Alexander Abdou,[1] Xing Haw Marvin Tan,[2,3,14] Alexei Christodoulides,[1] Carly M. Farris,[10,11] Changhoon Lee,[12] Pei-Yu Chiou,[2,3] Erica K. Sloan,[8,9] Parag Katira,[10,11] and Amy C. Rowat[1,2,5,6,7,*]

[1]Department of Integrative Biology and Physiology, University of California, Los Angeles, Los Angeles, CA, USA
[2]Department of Bioengineering, University of California, Los Angeles, Los Angeles, CA, USA
[3]Department of Mechanical and Aerospace Engineering, University of California, Los Angeles, Los Angeles, CA, USA
[4]Cousins Center for Psychoneuroimmunology, Semel Institute for Neuroscience and Human Behavior, University of California, Los Angeles, Los Angeles, CA, USA
[5]UCLA Jonsson Comprehensive Cancer Center, University of California, Los Angeles, Los Angeles, CA, USA
[6]Eli and Edythe Broad Center of Regenerative Medicine and Stem Cell Research, University of California, Los Angeles, Los Angeles, CA, USA
[7]California NanoSystems Institute, University of California, Los Angeles, Los Angeles, CA, USA
[8]Drug Discovery Biology Theme, Monash Institute of Pharmaceutical Sciences, Monash University, Melbourne, VIC 3052, Australia
[9]Division of Cancer Surgery, Peter MacCallum Cancer Centre, Melbourne, VIC 3052, Australia
[10]Mechanical Engineering Department, San Diego State University, San Diego, CA, USA
[11]Computational Science Research Center, San Diego State University, San Diego, CA, USA
[12]Department of Neuroscience, Peter O'Donnell Jr. Brain Institute, University of Texas Southwestern Medical Center, Dallas, TX, USA
[13]Department of Pathology, School of Medicine, University of New Mexico, Albuquerque, NM, USA
[14]Present address: Department of Electronics and Photonics, Institute of High-Performance Computing, Agency for Science, Technology and Research (A*STAR), Singapore, Singapore
[15]Lead contact
*Correspondence: takim@salud.unm.edu (T.-H.K.), rowat@ucla.edu (A.C.R.)
https://doi.org/10.1016/j.isci.2025.112676

SUMMARY

The ability of cancer cells to deform and generate force is implicated in metastasis. We previously showed that β-adrenergic agonists increase cancer cell stiffness, which was associated with enhanced motility and invasion. Here, we investigate how β-adrenoceptor (βAR) activation alters the mechanical behaviors of triple-negative breast cancer cells. We find that βAR activation increases traction forces in metastatic MDA-MB-231^{HM} and MDA-MB-468 cells, but not in non-tumorigenic MCF10A cells. Using computational modeling, we show that βAR activation increases the number of active myosin motors via myosin light chain phosphorylation. To identify molecular regulators, we use a deformability assay to screen for pharmacologic and genetic perturbations. Our results define a βAR-RhoA-ROCK-non-muscle myosin II (NMII) signaling axis that modulates the mechanical behaviors of MDA-MB-231^{HM} and MDA-MB-468 cells. These findings provide insight into how stress signaling regulates cancer cell mechanics and suggest potential targets to block metastasis in triple-negative breast cancer.

INTRODUCTION

Cellular mechanical behaviors are implicated in multiple steps of the metastatic cascade. The ability of cancer cells to deform and generate physical forces is required during intravasation as cancer cells escape from the primary tumor.[1] Indeed, cancer cells that exhibit increased traction forces tend to be more invasive.[2] Various factors in the tumor microenvironment are known to modulate cancer cell mechanical behaviors, including soluble and mechanical cues. In response to growth factors such as TGF-β, cancer cells increase their stiffness[3] and traction forces.[4] Mechanical cues, such as increased matrix stiffness in tumors, also cause cancer cells to increase their force production.[2] Cells can rapidly modulate their mechanical behaviors in response to extrinsic factors through changes in post-translational modifications, intracellular tension, and cytoskeletal organization.[5,6] Changes in mechanical behaviors can also be induced by altered gene expression, albeit on longer timescales of hours to days.[7] While various soluble and mechanical cues are known to regulate cancer cell mechanical behaviors,[4,8–11] a complete mapping of mechanical regulators could provide fundamental insights into cancer progression and metastasis.

The catecholamine stress hormones, epinephrine and norepinephrine, are critical regulators in physiology and disease. Acute

This is an open access article under the CC BY-NC-ND license (http://creativecommons.org/licenses/by-nc-nd/4.0/).

psychological stress rapidly increases local or circulating plasma concentrations of catecholamines, which results in increased activation of β-adrenoceptors (βAR); these G-protein coupled receptors are expressed in many types of cancers.[12–14] We previously discovered that activation of βAR regulates the deformability of a range of cancer cell types from breast to prostate, making cells stiffer or less deformable; this stiffer mechanotype induced by βAR activation is associated with increased cell motility and invasion.[15] The increased invasion of cancer cells induced by βAR activation is consistent with preclinical findings that activation of βAR signaling in response to agonists or physiological stress drives metastasis of breast cancer in mouse models.[16–18] Moreover, prospective clinical trials show that blocking βAR signaling with the clinically used β-blocker propranolol reduces biomarkers for metastatic potential and recurrence in breast cancer patients,[19,20] and also improves survival in melanoma patients.[21] Retrospective studies also suggest the protective effects of β-blockade as indicated by increased survival of breast cancer patients who coincidentally were taking β-blockers at the time of cancer diagnosis.[22–24] Population-based cohort studies further show that long-term use of β-blockers is associated with reduced breast cancer-specific death[25] and improved survival in triple-negative breast cancer (TNBC) patients.[26] If we could define the molecular and biophysical mechanisms of βAR regulation of cancer cell mechanical behaviors, this would enable us to predict and control how cells sense and respond to stress hormone cues and also design more effective strategies to treat cancer.

The effects of βAR activation on cellular force generation and motility have been shown to vary across cell types. βAR agonists increase the contractility of cardiac myocytes[27] but cause relaxation of human airway smooth muscle cells.[28] Across epithelial cells, βAR activation increases the migration of bovine bronchial epithelial cells[29] but decreases migration in corneal epithelial cells and keratinocytes.[30–32] As the architecture of signaling pathways can differ across cell types,[33] it remains unclear how mechanical behaviors of breast cancer cells are modulated in response to βAR cues. Previous studies provide some clues into mechanisms of how βAR activation mediates cellular mechanical behaviors. We previously showed that βAR signaling in breast cancer cells increased cell stiffness and invasion due to activation of βAR at the cell surface by soluble agonists, and these changes in mechanical behaviors require filamentous (F-) actin, non-muscle myosin II (NMII) activity, and calcium.[15,34] In renal cancer cells, βAR activation has been shown to increase RhoA activity via RhoGEF signaling, and thereby increase the number of focal adhesions.[35] By contrast, in airway smooth muscle cells, βAR activation can reduce cellular contractility by decreasing myosin light chain (MLC) phosphorylation through either a βAR-cAMP-PKA axis that inhibits RhoA[36] or by reducing myosin light-chain kinase (MLCK) activity in a Ca^{2+}/calmodulin-dependent manner.[37] Taken together, these findings highlight the different mediators involved in translating βAR activation into changes in cellular mechanical behaviors, and reveal the gap in mechanistic knowledge of how breast cancer cells respond to stress hormone cues.

Here, we define the molecular mediators that regulate the mechanical behaviors of breast cancer cells—including traction stresses, deformability, and invasion—in response to βAR activation. We focus our studies on the TNBC cell lines including the highly metastatic variant MDA-MB-231^{HM} and MDA-MB-468 cells, as well as the non-tumorigenic MCF10A cells. To investigate how soluble βAR agonists regulate cellular mechanical phenotype, we measure key mechanical behaviors of breast cancer cells including cellular traction forces, or the magnitude of physical forces that cells exert on their substrate; levels of NMII activity, which are associated with cellular force production; and cellular deformability, which we define as the ability of cells to deform through micron-scale pores in response to applied pressure. To gain mechanistic insights into how βAR activation increases cellular traction forces, we use a computational model to determine the effects of βAR activation on the mechanisms of actomyosin-mediated force generation, including the number of NMII that interact with actin filaments to generate forces. To identify molecules that mediate the βAR-induced changes in cellular mechanical behaviors, we use a high throughput filtration platform, called parallel microfiltration (PMF), to screen the effects of pharmacologic and genetic perturbations on whole cell deformability. Finally, we assess the role of the identified molecular mediators in βAR-induced cancer cell motility by measuring the *in vitro* invasion of breast cancer cells using a 3D scratch wound assay. Our findings establish βAR-RhoA-ROCK-NMII as a signaling axis that mediates the traction forces, deformability, and invasion of MDA-MB-231^{HM} and MDA-MB-468 breast cancer cells.

RESULTS

βAR signaling modulates breast cancer cell mechanical behaviors

Our previous findings showed that different types of cancer cells—including breast, ovarian, prostate, and melanoma—become less deformable or stiffer with βAR activation.[15] In the current study, we aimed to determine how βAR regulates cellular traction stresses and define the mechanism of βAR-induced changes in tumor cell mechanical behaviors.

Since βAR activation alters the contractility of cardiac myocytes and human airway smooth muscle cells,[27,28] and more invasive cancer cells tend to have increased traction forces compared to less invasive cells,[2] we test the effects of βAR signaling on cellular force generation. To quantify cellular traction forces, we use two complementary traction force microscopy (TFM) methods: TFM-Pillars and TFM-Beads Assays (Figure 1A). To assess how βAR activation impacts cellular traction forces, we seeded MDA-MB-231^{HM} cells on an array of elastomeric pillars (TFM-Pillars assay) and treated cells with the βAR agonist isoproterenol for 24 h, as described in our previous work.[15] To quantify traction forces, we tracked displacements of gold microdisks embedded on the tips of the pillars. We found that activation of βAR signaling in MDA-MB-231^{HM} cells with isoproterenol for 24 h resulted in a ~2-fold increase in median traction forces from ~2 nN to ~4 nN per pillar ($p < 0.0001$); this increase in cellular traction forces was abrogated by the β-blocker propranolol. Propranolol itself had no effects on baseline cellular traction forces compared to vehicle (Figures 1B and 1C). To assess how βAR activation affects cellular traction forces

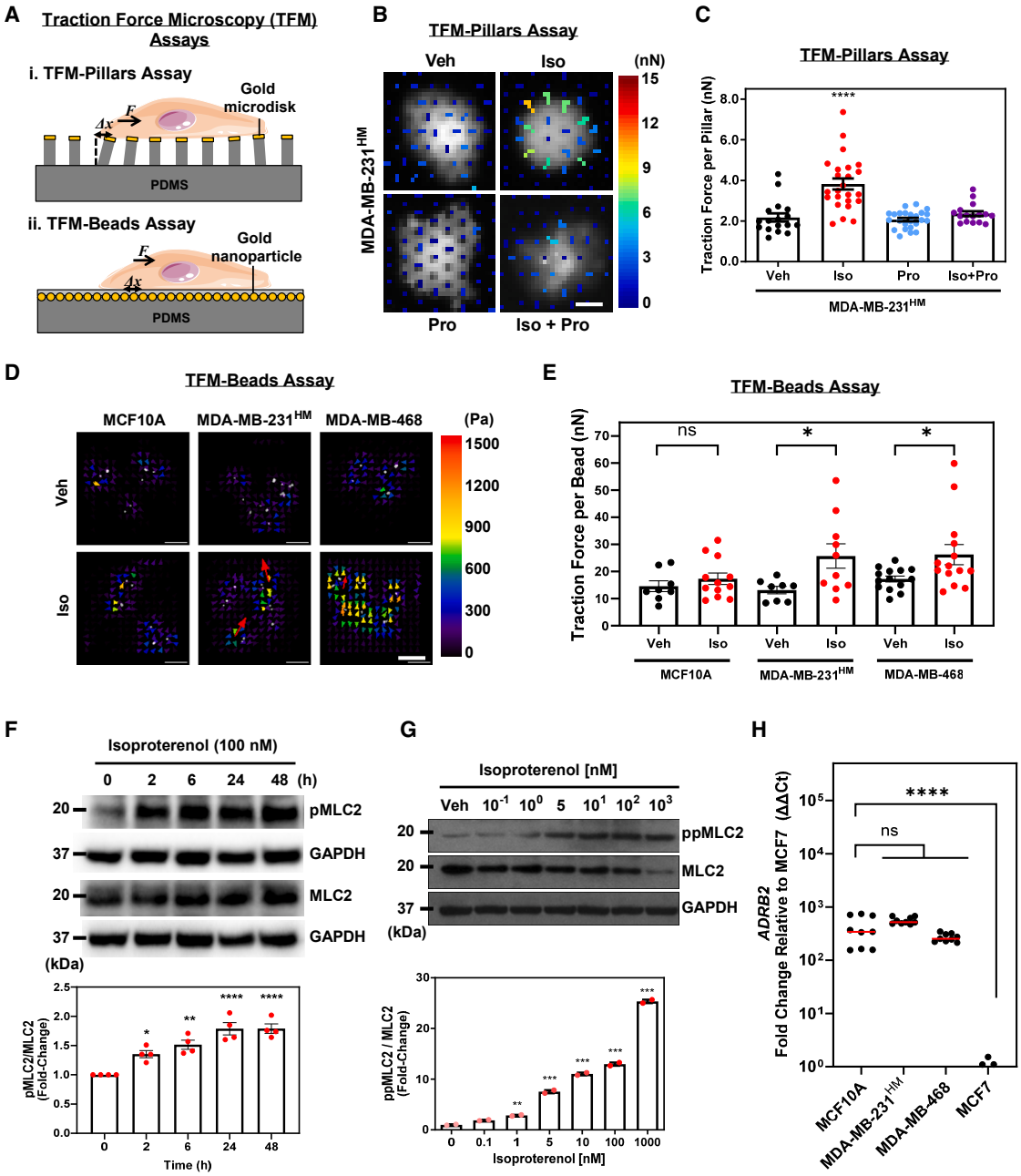

Figure 1. βAR activation results in increased cellular force generation

(A) Schematic illustration showing the traction force microscopy (TFM) assays. (i) TFM-Pillars Assay. Gold disks (yellow) are embedded on top of poly-dimethylsiloxane (PDMS) pillars to facilitate imaging lateral displacements due to cellular traction forces. (ii) TFM-Beads Assay. Gold nanoparticles (yellow) are embedded in a PDMS matrix to facilitate imaging lateral displacements due to cellular traction forces.

(B) Representative images of MDA-MB-231^{HM} cells on micropillars with superimposed vector force map. Color scale indicates the force per pillar. Scale, 4 μm.

(C) Traction forces of MDA-MB-231^{HM} cells using TFM-Pillars assay after treatment for 24 h with: vehicle, Veh; βAR agonist isoproterenol, Iso (100 nM); βAR antagonist propranolol, Pro (10 μM); or 100 nM Iso and 10 μM Pro. Each dot represents an individual pillar from at least 16 single cells across 3 independent experiments. Bars show the median; error bars represent standard error.

(D) Representative images from traction force measurements of TNBC and MCF10A cells treated with isoproterenol (Iso) for 24 h using the TFM-Beads assay. Each arrow indicates the direction of force and the color gradient corresponds to the magnitude of stress. Scale: 10 μm.

(E) Quantification of traction forces. Each data point represents the average traction force per bead for an individual cell, which is averaged over multiple beads that are within the boundary of each individual cell. Data shown here represent at least 7 individual cells across 3 independent experiments. Bars show the median; error bars represent standard error.

(legend continued on next page)

across other TNBC cells, we measured traction stresses of MDA-MB-468 cells as well as the non-tumorigenic MCF10A mammary epithelial cells by tracking displacements of gold nanoparticles embedded in an elastomeric substrate (TFM-Beads assay). To capture changes in contractility induced by βAR activation signaling rather than by changes in the expression level of βAR—which can be downregulated after 24 h of activation[38]—we measured traction stresses at an earlier 2 h timepoint. With both TNBC cells after 2 h of isoproterenol treatment, we found that activation of βAR signaling resulted in an increase in cellular traction forces. The MDA-MB-468 and MDA-MB-231^{HM} cells showed the most significant >1.5-fold increase in median traction force (Figures 1D and 1E). By contrast, the non-tumorigenic MCF10A cells showed no significant increase in contractility after βAR activation (Figures 1D and 1E). The differential response in cellular traction forces across cell lines could result from differences in basal expression levels of β-adrenergic receptors. We previously determined that β_2AR, which is encoded by *ADRB2*, is the predominant subtype in MDA-MB-231^{HM} cells, and β_2AR is required for cell stiffness changes induced by βAR activation.[15] However, we did not observe any statistically significant differences in levels of *ADRB2* transcripts between MCF10A and the TNBC cells, while MCF7 cells show lowest expression level (Figures 1H and S2A). Taken together, the trend of increased traction forces with βAR activation is consistent across timepoints, TFM assays, and TNBC cancer cell lines.

Since traction forces are regulated by NMII activity, we next measured phosphorylation of myosin light chain 2 (MLC2), which regulates NMII motor activity, the formation of myosin filaments, and actin-myosin crosslinking.[39] Both mono-phosphorylation, pMLC2 (S19), and di-phosphorylation, ppMLC2 (T18/S19), of MLC2 are associated with increased NMII activity and show similar kinetics upon activation.[40] We focused our studies on MLC2 phosphorylation in MDA-MB-231^{HM} cells, which showed the greatest change in contractility and deformability in response to βAR activation (Figure 2B). We found increased levels of pMLC2 at 2 h and up to 48 h after βAR activation, suggesting that βAR activation induces a sustained increase in NMII activity (Figure 1F). We also found that βAR activation by isoproterenol resulted in a concentration-dependent increase in the phosphorylation of MLC2 at 2 h (Figure 1G). With the same 100 nM isoproterenol concentration that induced an increase in cellular traction forces, we observed a ∼13-fold increase in MLC2 phosphorylation relative to total MLC2. Since βAR activation resulted in increased contractility and MLC2 activity of breast cancer cells compared to MCF10A cells (Figures 1D and 1E), we next assessed levels of transcripts for cellular contractility mediators—including non-muscle myosin heavy chains (*MYH9*, *MYH10*, and *MYH14*) and light chains (*MYL9*, *MYL12A*, and *MYL12B*)—in publicly available RNA-seq datasets for MDA-MB-231 and MCF-10A cells.[41] We found that *MYH9* encoding NMIIA and *MYL9* encoding MLC2 were expressed at significantly higher levels in MDA-MB-231 compared to MCF10A (Figures S2D and S2E).

We next assessed the effects of βAR activation on the deformability of the breast tumor cells, MDA-MB-231^{HM}, versus the non-tumorigenic mammary epithelial cells MCF10A following treatment with the βAR agonist isoproterenol. To measure whole-cell deformability, we used the PMF method that we previously developed,[42] which measures the ability of whole cells to passively deform through 10 μm pores on the timescale of seconds. Less deformable cells are more likely to occlude the pores, resulting in reduced filtration and increased retention of the cell suspension in the top well (Figure 2A). We focused our studies of βAR activation on the deformability of cells treated using 100 nM isoproterenol, which we previously found induces maximal changes in deformability of MDA-MB-231^{HM} cells[15] and is below 1 μM isoproterenol that has been reported to reduce the proliferation of MDA-MB-231 cells.[43] Our findings show that the highly metastatic MDA-MB-231^{HM} cells showed an increase in retention with 100 nM isoproterenol treatment (Figure 2B); this was consistent with our previous reports.[15] By contrast, we found no significant changes in the retention of MCF10A cells following βAR activation. We also did not observe any significant changes in cell or nuclear size across treatment conditions (Figures S1A and S1G), indicating that the observed differences in retention of MDA-MB-231^{HM} cells with isoproterenol treatment were not due to changes in cell size. We found no significant differences in cell viability or apoptosis (Figure S3), thereby excluding cell death or apoptosis as the origin of the altered cell deformability. We also found that the increased retention caused by isoproterenol was abrogated by treatment with the βAR antagonist propranolol, confirming that isoproterenol is acting through βAR (Figure 2B). These findings suggest that βAR activation alters the deformability of MDA-MB-231^{HM} cells but not of non-tumorigenic MCF10A cells.

βAR activation increases cellular force generation by enhancing actin-NMII binding

To gain mechanistic insight into how stress hormones regulate cellular mechanical behaviors, we employed a computational model[44] which integrates chemo-mechanical regulation of the following elements: (1) individual myosin motors as they interact with associated actin filaments; (2) focal adhesion formation between substrate-bound integrin, talin, and vinculin-capped actin filaments; (3) force generation via myosin interactions with integrin-bound actin filaments; (4) force transmission

(F) Western blotting against mono-phosphorylated myosin light chain 2 (pMLC2), non-phosphorylated MLC2, and GAPDH from MDA-MB-231^{HM} cells treated with 100 nM of isoproterenol for up to 48 h. Quantification of band intensity for pMLC2/MLC2 was normalized to 0 h sample.
(G) Western blotting against di-phosphorylated MLC2 (ppMLC2), non-phosphorylated MLC2, and GAPDH after MDA-MB-231^{HM} cells were treated with increasing concentrations of isoproterenol for 2 h. The ratio of ppMLC2 to MLC2 was normalized to vehicle control.
(H) Expression levels of *ADRB2* transcripts in TNBC, MCF10A, and MCF7 cells measured by qRT-PCR. Images in (A) are adapted from Servier Medical Art by Servier and are published a Creative Commons BY license (https://creativecommons.org/licenses/by-nc/3.0/). Unless otherwise stated, all error bars represent mean ± s.e.m (N = 3). *p < 0.05; **p < 0.01; ***p < 0.001 [one-way ANOVA with Tukey's test (F–H) and statistical significance in (C and E) is determined using a permutation test to evaluate the difference in medians between control and treatment conditions. *p < 0.05].

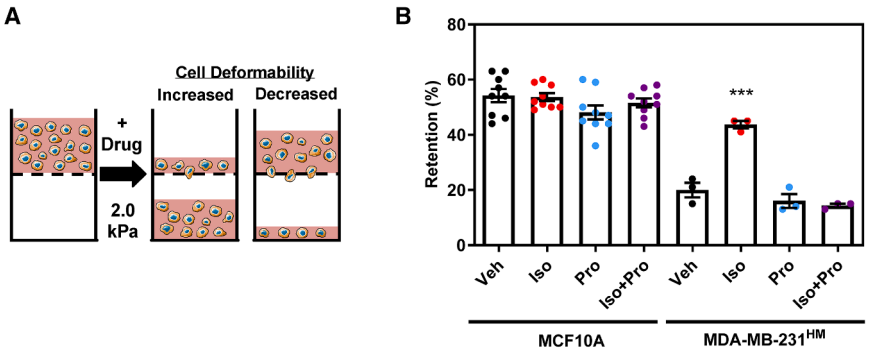

Figure 2. βAR activation results in decreased cancer cell deformability

(A) Schematic illustration showing the PMF assay. Suspensions of cells were loaded into the top well separated with porous membranes from the bottom well.

(B) Filtration measurements by PMF reveal cellular deformability of non-transformed epithelial cells (MCF10A) versus triple-negative breast cancer cells (MDA-MB-231) and the highly metastatic variant of MDA-MB-231 cells (MDA-MB-231^{HM}) after treatment for 24 h with: vehicle, Veh; βAR agonist isoproterenol, Iso (100 nM); βAR antagonist propranolol, Pro (10 μM); or 100 nM Iso and 10 μM Pro. All error bars represent mean ± s.e.m ($N = 3$). *$p < 0.05$; **$p < 0.01$; ***$p < 0.001$ [one-way ANOVA with Tukey's test]. Images in A are adapted from Servier Medical Art by Servier and are published under a Creative Commons BY license (https://creativecommons.org/licenses/by-nc/3.0/).

across the focal adhesion to the substrate; and (5) force-dependent dynamics of focal adhesion disassembly via the breaking of integrin-substrate catch-slip bonds. Additional key features and the underlying equations that describe the interactions between the various elements of the model are provided in the STAR Methods (Equations 1, 2, 3, 4, 5, 6, 7, and 8). Using this model, we estimated the force in individual actin-myosin filaments over time as they bind, tug, and unbind from surface bound integrins (Figure S6). We also determined the net traction force per unit area generated within focal adhesions over time. The effect of isoproterenol on traction force generation is assessed by calculating the ratio of transition rates of myosin motors between an inactive state and an active state from the experimentally determined ratios of ppMLC/MLC (Figure 1D; Equation 1 in STAR Methods). Increasing isoproterenol concentration from 0 to 1,000 nM resulted in a 4-fold increase in the number of NMII that are actively interacting with actin filaments and generating forces (Figure 3B). Consequently, the net predicted traction force per unit area also increased by approximately 2.5-fold for isoproterenol concentrations >10 nM (Figure 3C), in close quantitative agreement with the experimental traction force data (Figures 1B and 1C). This increase in net traction force is an outcome of a 5-fold increase in the force generated within each individual actin-myosin filament due to higher numbers of interacting NMII per filament in response to βAR, and a slight decrease in the focal adhesion lifetimes connecting the filaments to the substrate (Figures 3D and S5A–S5C).

To illustrate how this mechanism of cellular force generation contrasts the cellular response to matrix stiffness, which is established to increase cellular traction forces,[45,46] we used the same model to predict traction forces with increasing substrate stiffness (increasing the value of effective k_{spring} in the model). We observed that with increasing substrate stiffness, the increased traction forces at focal adhesions result from a stronger force generated within a single actin filament due to increased cooperativity between the motors while the number of interacting motors remains the same (Figures S4A–S4C and S5D–S5F).[44,47] These observations are consistent with previous models of cellular traction force generation with increasing substrate stiffness.[48]

While this minimal model neglects downstream effects of focal adhesion signaling in modeling the response to cells to both βAR activation and matrix stiffness, the results obtained are aligned with the experimental observations of βAR activation, indicating that we are capturing the predominant mechanisms of traction force generation. Both modeling and experimental data show increased cellular traction forces in 2D (Figures 1 and S5A); and the increase in myosin-generated force per individual actin filament should translate to increased contraction and migration speed in 3D environments, as our previous work shows.[49] Taken together, these data from both computational modeling and experiments substantiate that βAR activation increases force generation in MDA-MB-231^{HM} breast cancer cells by MLC2 phosphorylation and a consequent increase in the number of active motors per actin filament.

βAR signaling alters cell deformability through a RhoA-ROCK-NMII axis

To begin to dissect the molecular mechanisms underlying how βAR increases NMII activity to regulate breast cancer cell mechanical behaviors, we tested the role of specific kinases that may be involved in βAR regulation of NMII activity using pharmacologic inhibitors. We activated βAR signaling while simultaneously inhibiting the activity of three kinases that are well-characterized regulators of NMII activity: Rho-Associated Kinase (ROCK), Myosin light-chain kinase (MLCK), and p21-activated kinase 1 (PAK1), using the pharmacologic inhibitors Y27632, ML-7, and IPA-3. We used PMF to rapidly assay effects of these perturbations on βAR regulation of the deformability of MDA-MB-231^{HM} cells.[42] Activating βAR by isoproterenol treatment resulted in a significant increase in retention (as in Figure 2B). However, when ROCK was inhibited by Y27632, isoproterenol treatment did not cause any significant increase in retention, suggesting that ROCK activity is required for the βAR-induced decrease in cellular deformability. By contrast, when MLCK and PAK1 were inhibited by ML-7 and IPA-3, we still observed a statistically significant increase in retention following isoproterenol treatment (Figure 4A). Taken together, these findings indicate that ROCK is a major contributor to the βAR-induced changes

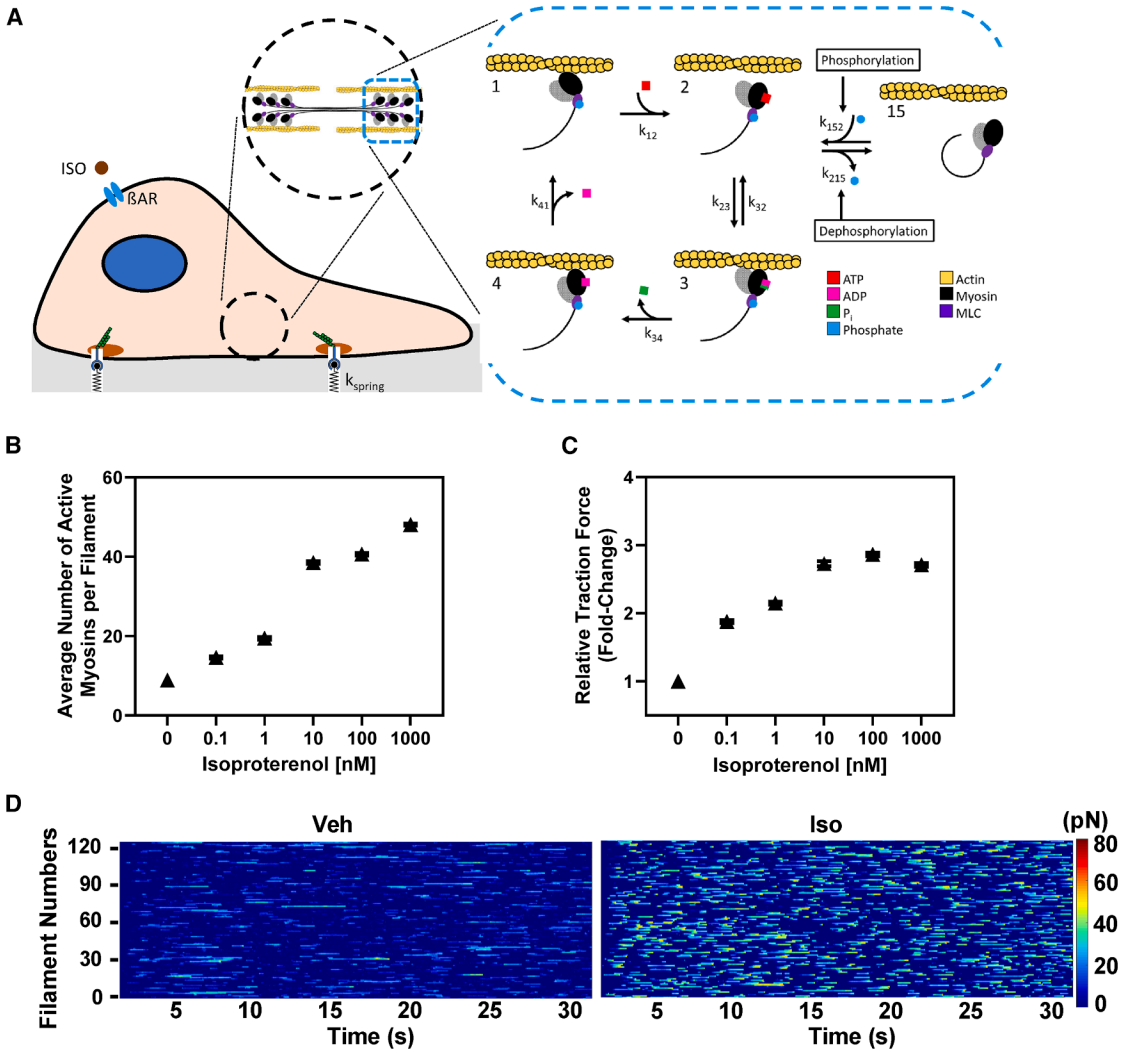

Figure 3. βAR activation increases the number of NMII motors interacting with F-actin to yield increased traction force generation

(A) A stochastic Monte Carlo model is used to simulate the state transitions and force generation in actin-myosin filaments that are transferred to the substrate via integrins. Schematic shows actomyosin complex attaching to integrin on the cytosolic side. Endogenous forces affect integrin bond lifetime, which is modeled by a spring with catch-slip dynamics.

(B) Simulations predict the number of active NMII motors per actin filament (for a maximum of 60 NMII per actin filament and 120 actin filaments per μm^2) with increasing concentrations of isoproterenol, [Iso]; 0 nM isoproterenol is vehicle control.

(C) Traction forces per μm^2 predicted by simulation are normalized to vehicle control.

(D) Kymographs show simulated forces at focal adhesions. Each row represents an individual actin-myosin filament and summation over all 120 filaments (rows) represents the total traction force at time (*t*). Color map gradient shows magnitude of force generated at focal adhesion.

in cellular deformability. We validated these findings by treating cells with increasing concentrations of isoproterenol in the presence of each myosin kinase inhibitor; the βAR-induced increase in retention was fully blocked only when ROCK activity was inhibited by Y27632 (Figures 4B–4D). We observed similar effects with the ROCK inhibitor, g-H-1152, which has higher specificity for ROCK than Y27632[50] (Figure 1E). Across all treatments, we found no significant differences in cell viability or apoptosis (Figure S3), which can result in increased cell stiffness.[51] We further assessed myosin activity by measuring pMLC2 levels in MDA-MB-231^{HM} cells after βAR activation with or without inhibition of each myosin kinase using western blotting. Consistent with the PMF data, we observed that βAR-induced myosin activation was blocked most significantly when ROCK was inhibited (Figures 4E and 4F), suggesting that ROCK is required to translate βAR signaling into changes in cancer cell mechanical behaviors. These results show that ROCK activity is required for βAR regulation of the deformability of MDA-MB-231^{HM} cells, indicating the role of ROCK in mediating the mechanical behaviors of MDA-MB-231^{HM} cells with βAR activation.

We next investigated the role of RhoA—a canonical upstream regulator of ROCK and NMII activity—in regulating βAR-induced changes in cellular deformability using genetic

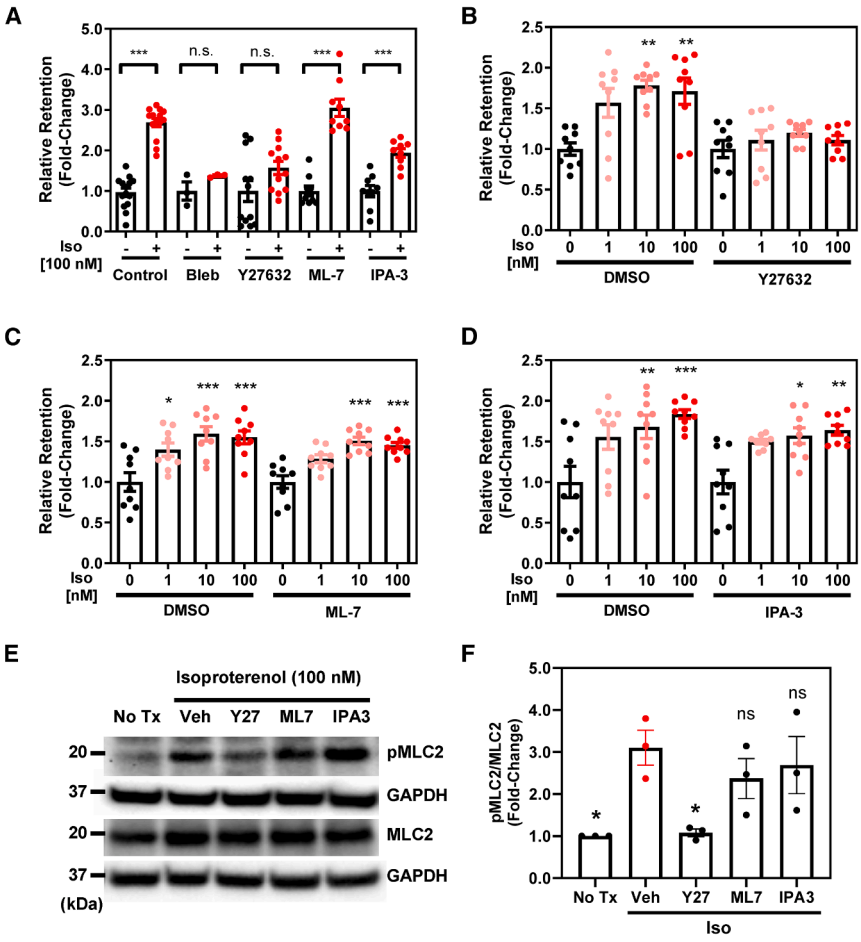

Figure 4. βAR-induced changes in cellular deformability require ROCK activity

(A) Cell filtration measurements by PMF with simultaneous βAR activation by isoproterenol (Iso) and suppression of myosin activity by pharmacological inhibitors, Bleb, blebbistatin (10 μM); Y27632 (10 μM); ML-7 (10 μM); and IPA-3 (10 μM). Cells were co-treated with inhibitors and isoproterenol for 24 h prior to filtration measurements.

(B–D) Filtration measurements with increasing concentration of isoproterenol with or without NMII-regulating kinase inhibitors.

(E) Western blotting against phosphorylated MLC2 (pMLC2), non-phosphorylated MLC2, and GAPDH.

(F) Normalized ratio of pMLC2 to MLC2 levels after MDA-MB-231^{HM} cells were treated with isoproterenol with or without inhibition of ROCK (Y27632), MLCK (ML7), and PAK1 (IPA3). Data represents 3 independent experiments. n.s.: not significant, $^{*}p < 0.05$; $^{**}p < 0.01$; $^{***}p < 0.001$ [one-way ANOVA with Tukey's test].

and pharmacological approaches. RhoA regulates actomyosin contractility and stress fiber formation via effector proteins, ROCK1/2 and DIA1/2.[52,53] Knockdown of RhoA by two different siRNAs (siRhoA-1 and siRhoA-2) reduced protein levels by ~70% (Figures 5A and 5B). Cells with RhoA knockdown did not show any observable increase in retention following βAR activation (Figure 5C); these findings were consistent with the effects of ROCK inhibition (Figures 4A, 4B, and S1E). To activate RhoA, we treated cells with Rho Activator II, CN03, which specifically activates Rho GTPase isoforms; Rac1 and Cdc42 GTPases are not affected. Indeed, cells treated with increasing concentrations of CN03 showed increased retention, indicating decreased deformability (Figure 5D). No differences in cell size were observed after CN03 treatment (Figure S1F). To determine if differences in expression of mediators in the RhoA-ROCK-NMII axis could contribute to the observed differential response in cellular mechanical behaviors, we analyzed publicly available gene expression data. Gene expression analysis revealed higher transcript levels of *RHOA* in MDA-MB-231 than MCF10A cells, with no significant differences in *ROCK1* and *ROCK2* expression levels (Figures S2B and S2C). A higher basal expression of *RHOA* could also contribute to a stronger activation of a βAR-RhoA-ROCK axis in TNBC cells compared to non-tumorigenic cells. Since ROCK phosphorylates the myosin binding subunit of myosin phosphatase and inhibits phosphatase activity resulting in increased levels of phosphorylated MLC, which increases NMII activity, we next assessed the effects of direct inhibition of NMII activity by treating cells with blebbistatin prior to isoproterenol treatment; this also resulted in no significant change in retention, which is consistent with our previous report[15] (Figure 4A). Taken together, our findings support that βAR activation alters breast cancer cell deformability through a RhoA-ROCK-NMII axis.

βAR signaling regulates cancer cell invasion through a RhoA-ROCK-NMII axis

Since cellular mechanical behaviors including motility contribute to tumor cell invasion which is important in cancer metastasis,[15,54–56] we next investigated the role of a RhoA-ROCK-NMII axis in regulating the βAR-induced changes in the invasion of breast cancer and non-tumorigenic mammary epithelial cells. To simulate invasion through the tissue environment and validate our findings in a 3D context, we used a 3D Matrigel scratch wound assay.[15,57] We found that isoproterenol treatment resulted in increased invasion of MDA-MB-231^{HM} cells compared to vehicle treated cells (Figures 6A–6C, 6E, 7A, and 7B); this finding was consistent with our previous studies.[15] By contrast, the invasion of MCF10A cells with βAR activation was not significantly altered (Figures 7C and 7D). With inhibition of NMII activity (blebbistatin) or ROCK (Y27632), βAR activation had no observable effects on the invasion of MDA-MB-231^{HM} cells (Figures 6A–6C and 6E). We next tested the effects of RhoA on βAR modulation of cancer cell invasion. We found that RhoA is required for the βAR-mediated increase in cell invasion (Figures 6B and 6D): siRhoA

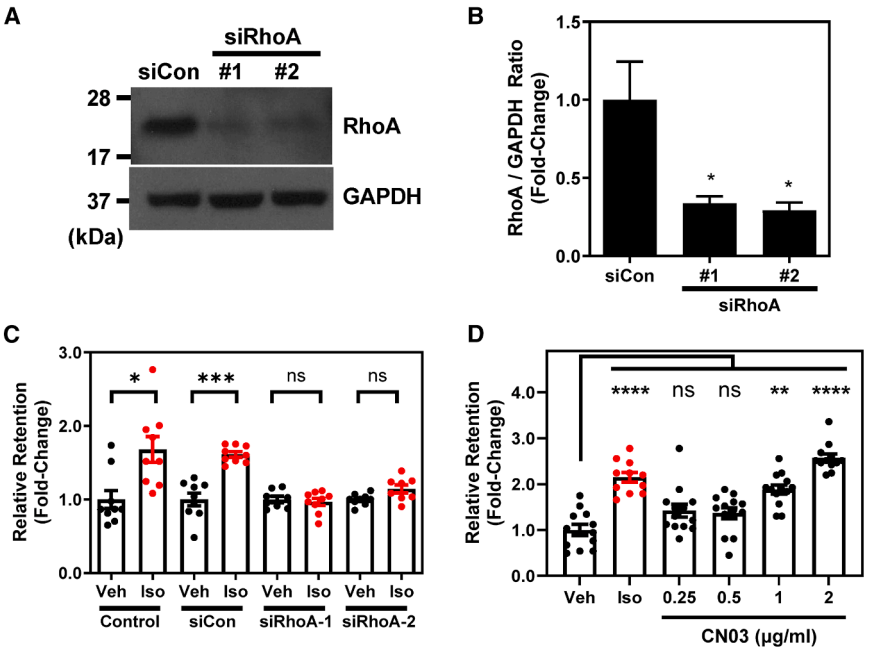

Figure 5. RhoA contributes to βAR regulation of cellular deformability

(A) Confirmation of siRNA knockdown of RhoA by western blotting. GAPDH is loading control.

(B) Ratio of RhoA to GAPDH normalized to control siRNA (siCon).

(C) Cell filtration with PMF after 100 nM of isoproterenol treatment for 24 h in control and RhoA knockdown cells.

(D) Cell filtration with PMF after increasing concentration of Rho activator, CN03, treatment for 4 h. Multiple comparisons from ANOVA test were made by comparing the mean of each treatment with the mean of Veh treatment. All experiments were performed 3 times ($N = 3$). n.s.: not significant, $^{*}p < 0.05$; $^{***}p < 0.001$ [one-way ANOVA with Tukey's test].

knockdown blocks the increased invasion with isoproterenol treatment (Figure 6F); consistent with this finding, RhoA activation by CN03 increased the invasion of MDA-MB-231^{HM} cells (Figures 7A and 7B). Simultaneous activation of βAR and RhoA with isoproterenol and CN03 co-treatment did not show any synergistic effects on invasion, suggesting that RhoA is a downstream effector in βAR-induced cell invasion. By contrast, activation of βAR signaling in MCF10A cells resulted in no change in cell invasion (Figures 7C and 7D), consistent with our traction force (Figures 1D and 1E) and deformability results (Figure 2B). Surprisingly, RhoA activation by CN03 in MCF10A cells resulted in decreased cell invasion (Figures 7C and 7D). Since cell proliferation can also impact wound closure rates in this 3D invasion assay, we measured changes in cell confluence over the experimental timescale of 48 h but found no significant changes across inhibitor treatments and RhoA knockdown (Figures S1B and S1C). These findings demonstrate that the increased invasion by βAR activation in MDA-MB-231^{HM} cells is associated with the changes in cellular mechanical behaviors—reduced deformability and increased contractility—that are mediated by ROCK, RhoA, and NMII activity. The breast cancer cell line MDA-MB-468 shows similar increased traction forces with βAR activation. Further studies will confirm how these findings can be extended to other subtypes of breast cancer cells, and more broadly other types of cancers.

DISCUSSION

Here, we show that a βAR-RhoA-ROCK-NMII axis plays a central role in how MDA-MB-231^{HM} breast cancer cells translate soluble stress hormone cues into changes in cellular mechanical behaviors, including their contractility and deformability, as well as invasion (Figure 8). We also show that βAR signaling increases traction force generation in the additional TNBC cell line, MDA-MB-468. Further validation with additional TNBC cell lines and patient samples will determine how broadly βAR activation mediates the mechanical behaviors of TNBC cells. By contrast, we find that non-tumorigenic mammary epithelial MCF10A cells do not show any change in traction forces or deformability with βAR activation.

Mechanistically, our findings show that βAR agonists increase cellular force production through a RhoA-ROCK–dependent increase in MLC2 phosphorylation and increase in the number of NMII motors engaged with actin; this mechanism contrasts the increased force production in response to increased matrix stiffness, which occurs due to increased forces generated by individual actin filaments independently of the number of active motors. The ability of cells to increase force production through two separate yet complementary mechanisms could enable them to independently tune force production to achieve enhanced sensitivity and/or dynamic range in response to combinations of external cues.

The βAR-RhoA-ROCK-NMII axis is one of a growing number of axes that are recognized to modulate cellular mechanotype.[58,59] A RhoA-ROCK axis has been implicated in how tumor cells remodel their tumor microenvironment,[60] resist fluid shear stresses,[61] and sense matrix stiffness through integrin signaling.[62] ROCK is also involved in how cancer cells sense and respond to the increased matrix stiffness that results from fibrosis and cancer-associated fibroblast contractility.[63] It will be important to further define the extent to which βAR activation of the RhoA-ROCK signaling axis compares to other growth factor or GPCR signaling pathways. For example, we showed that elevated levels of intracellular cAMP by high extracellular glucose increased the stiffness and motility of human TNBC cell lines.[11] Since βAR also increases intracellular cAMP levels,[15] we speculate that any upstream signaling events that utilize cAMP as a secondary messenger may regulate cell mechanical behaviors via a RhoA-ROCK axis in a cell type-dependent manner. Other essential factors in the tumor microenvironment such as epidermal growth factors can also modulate cancer

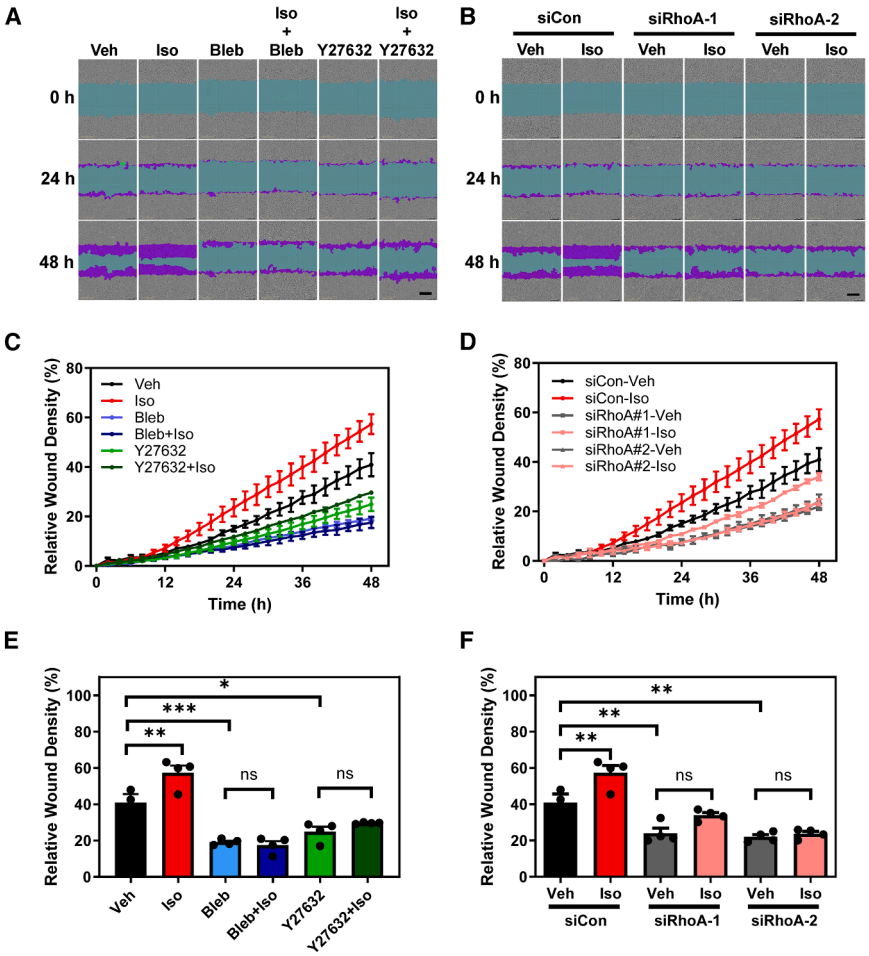

Figure 6. NMII, ROCK, and RhoA activity are required for the increased invasion of MDA-MB-231^{HM} cells due to βAR activation

(A and B) Representative images from a 3D scratch wound invasion assay. The confluent cells appear gray; the scratch wound is teal; and the cells that enter the scratch wound are represented with purple. Drugs were added at time 0: isoproterenol (Iso, 100 nM), NMII inhibitor blebbistatin (Bleb, 10 μM), and ROCK inhibitor Y27632 (10 μM). Transfections were performed 72 h prior to time 0 h of the invasion assay. Scale: 300 μm.

(C and D) Relative wound density as a function of time. Relative wound density is defined as the area of cells in the newly healed scratch wound region (purple) compared to the area of the initial scratch wound (teal at time 0 h).

(E and F) Relative wound density at 48 h. Unless otherwise indicated, all comparisons were made to vehicle control (Veh). All experiments were performed 3 times (N = 3). n.s.: not significant, $^{*}p < 0.05$; $^{**}p < 0.01$; $^{***}p < 0.001$ [one-way ANOVA with Tukey's test].

cell mechanical behaviors including local cell elasticity, actin cytoskeleton architecture, and cell migration.[10] It will be interesting in future work to define the interplay among multiple signals that activate RhoA-ROCK[64] to regulate cancer cell behaviors in the complex tumor microenvironment.

To gain mechanistic insight into how βAR activation increases cellular force generation, we applied a detailed chemo-mechanical model of actin-myosin force generation and cellular traction, which fully captures the observed βAR-induced increase in cellular traction forces. Further extensions of the model could predict the effects of soluble cues on more complex cellular behaviors such as motility and bi-directional cell-matrix interactions. Indeed, previous studies report that βAR activation impacts focal adhesion kinase (FAK) activity[65] and focal adhesion size,[17] suggesting there may be interplay between βAR signaling and cell-matrix interactions that are mediated through integrins. It will thus be valuable to determine how mechanical cues—such as integrin engagement[66,67] and/or spatial distribution of adhesions—might impact the sensitivity of cells to soluble stress hormone cues.

Our findings provide mechanistic insight into the relationship between cell contractility, deformability, and invasion. We posit that cancer cells tend to be inherently more deformable at baseline compared to non-transformed cells: Malignant transformation is typically accompanied by major changes in cytoskeletal remodeling, which render cells more deformable. In many contexts, more invasive cancer cells tend to be more deformable, as shown across pancreatic, breast, and ovarian cancer cell lines.[54–56,68–71] These findings are consistent with our observations that without any βAR perturbation, MDA-MB-231^{HM} cells are more deformable (Figure 2B) than the non-tumorigenic, less invasive MCF10A cells. Upon βAR activation, the increased NMII activity and force generation causes MDA-MB-231^{HM} cells to be transiently *stiffer* and *more invasive*. By contrast, MCF10A cells show no significant change in force generation or deformability with βAR activation. We postulate that the higher transcript levels of key regulators of cellular contractility—including *RHOA* and non-muscle myosin (*MYH9* and *MYL9*)—in MDA-MB-231 cells compared to MCF10A cells may contribute to the change in cellular mechanical behaviors elicited by βAR activation (Figures S2B–S2E).

While our findings here suggest that increased NMII activity contributes to the simultaneous increase in cell stiffness and invasion, this mechanism is likely to be also context dependent. Different types of cells may utilize different mechanisms to regulate their force generation or deformability; for example, MCF10A cell stiffness is sustained by actin polymerization, whereas the stiffness of MDA-MB-231 cells is largely determined by myosin II activity.[72] Cells can also rely on different modes or mechanisms of invasion, some of which require NMII activity, but others that utilize other force-generating mechanisms involving Arp2/3 or formins.[73–77] Thus, while we found that βAR activation enhanced RhoA-ROCK signaling to increase breast cancer cell invasion, βAR activation may have reduced effects on invasion

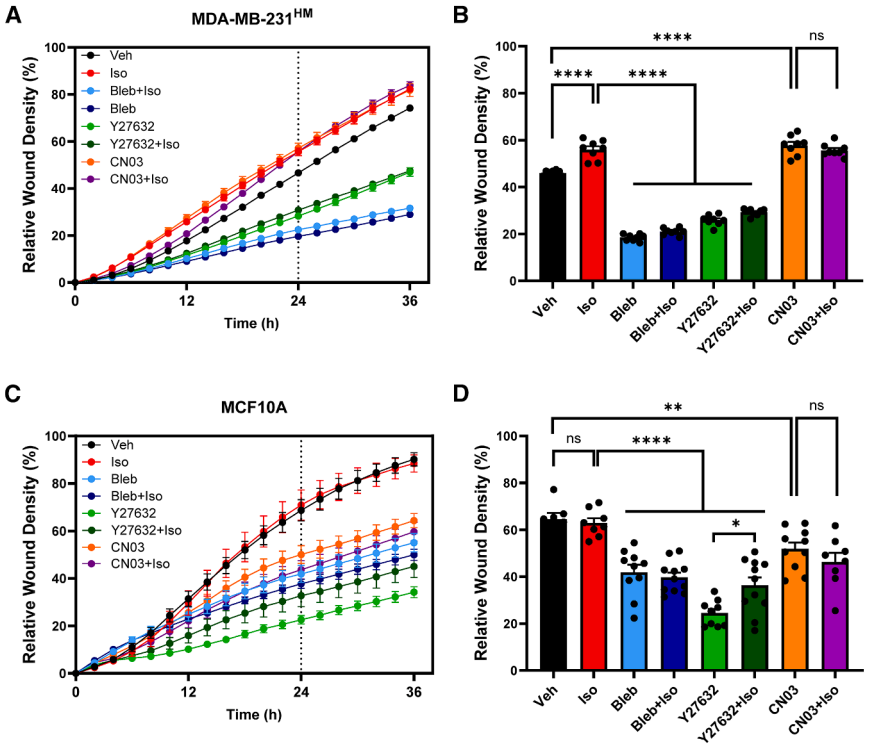

Figure 7. NMII and ROCK activity are required for invasion of MDA-MB-231^{HM} and MCF10A cells, while βAR activation increases invasion of MDA-MB-231^{HM} cells only

3D scratch wound invasion assays from MDA-MB-231^{HM} (A), and MCF10A (C) cells treated with isoproterenol (Iso, 100 nM), NMII inhibitor blebbistatin (Bleb, 10 μM), ROCK inhibitor Y27632 (10 μM), and Rho activator CN03 (1 μg/mL).

(B and D) Relative wound density at 24 h. Unless otherwise indicated, all comparisons were made to vehicle control (Veh). All experiments were performed 3 times (N = 3). n.s.: not significant, $^{*}p < 0.05$; $^{**}p < 0.01$; $^{***}p < 0.001$ [one-way ANOVA with Tukey's test].

when cells rely on a different mode of motility, such as Arp2/3-dependent invasion.[78] Analysis of expression levels of "mechanome" proteins that regulate mechanical processes may provide further mechanistic insight into the differential effects of βAR activation on different cell types. Considering that cell invasion typically occurs over timescales of ~1–100 h, which is similar to timescales of protein level changes, βAR regulation of proteins that determine cell-matrix interactions (such as integrins) or that degrade the extracellular matrix (such as matrix metalloproteinases, MMPs), could also contribute to cell invasion.[79] It will be important in future studies to prioritize factors that regulate cellular mechanical behaviors upon βAR activation from transcriptional and post-translational levels to functional behaviors across cell types.

The molecular mediators upstream of RhoA that determine βAR-mediated regulation of mechanotype remain to be determined. The effects of βAR agonists on cellular mechanotype have been well-studied in heart muscle cells, where β_1AR is the dominant receptor subtype,[80] as well as in human airway smooth muscle cells, which express only β_2AR.[81] In the breast cancer epithelial cells we investigate here, β_2AR is the predominant receptor subtype[17,82] and is required for the βAR-induced changes in the deformability of MDA-MB-231^{HM} breast cancer cells.[15] Future studies will determine the role of specific receptor subtypes in regulating cellular mechanical behaviors, as well as differences in signaling pathways that regulate mechanotype responses across different types of cells. The exact downstream effectors of βAR that contribute to regulating mechanical behaviors of breast cancer cells also remain to be defined. Our previous findings support that βAR-regulation of cellular mechanotype involves cAMP because treatment with the adenyl cyclase activator forskolin similarly resulted in decreased cellular deformability.[15] These findings are consistent with previous reports that βAR regulates cellular functions through the canonical G protein-mediated cAMP-PKA signaling pathway,[83] but the exact downstream effectors of βAR that contribute to regulating mechanical behaviors of breast cancer cells are not yet elucidated. βAR is also known to regulate cellular behaviors through β-Arrestin across multiple types of cells and tissues.[84–86] β-Arrestin is implicated in regulation of cellular mechanotype through a β-Arrestin-Src pathway,[87,88] as well as through a β_2AR-β-Arrestin2/RhoGEF-RhoA axis that was identified in renal

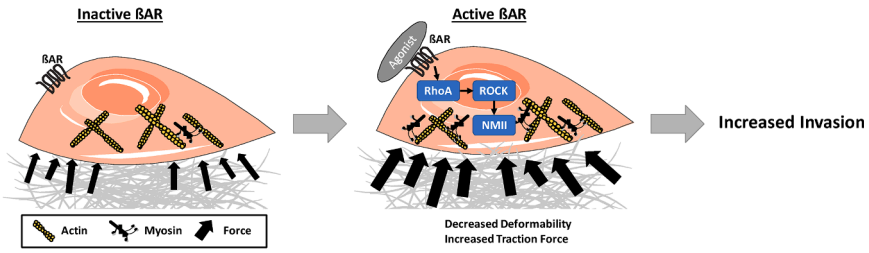

Figure 8. Schematic illustration of the proposed mechanism for how a βAR-RhoA-ROCK-NMII axis regulates mechanical behaviors of TNBC cells that can contribute to metastasis

Actin filaments are shown in yellow and myosins attached to these filaments are shown in black. Black arrows indicate traction forces generated by the cell. Images are adapted from Servier Medical Art by Servier (http://www.servier.com/Powerpoint-image-bank) and are published under a Creative Commons by license (https://creativecommons.org/licenses/by-nc/3.0/).

cancer and human embryonic kidney cells.[35] The extent to which β-Arrestin is involved in βAR regulation of breast cancer cell deformability and invasion remains to be defined. The role of specific ROCK isoforms in βAR-regulation of mechanotype also remains to be determined, including whether ROCK1/2 have redundant roles. Previous reports identify that ROCK isoforms differentially modulate cancer cell motility in MDA-MB-231 cells,[62] so we anticipate that specific isoforms may also differentially modulate cellular mechanotype. While we show here that RhoA-ROCK is a major axis for activating NMII through βAR, additional pathways that regulate NMII activity, such as MLCK and PAK, may also be involved in βAR-regulation of cancer cell mechanotype through compensatory effects and/or crosstalk with the RhoA-ROCK signaling pathway. Understanding the interplay among diverse signaling pathways that regulate cancer cell invasion and metastasis will also be crucial; for example, βAR activation affects downstream mediators including Src and MMPs, which are established to promote metastasis.[87–90] Combinatorial studies that utilize co-treatments of inhibitors and/or knockdowns will further refine our mapping of the specific pathways that contribute to βAR regulation of cellular mechanotype.

Future studies across a broader range of malignant and non-transformed epithelial cell types will be valuable to define how broadly a βAR-RhoA-ROCK-NMII axis is involved in regulation of mechanotype across different types of cells. Beyond cancer, βAR signaling impacts the mechanical behaviors of cell types across organ systems, from increasing the contractility of cardiac myocytes[91] to decreasing the traction stresses of human airway smooth muscle cells.[92] Recent findings show that activating βAR in adipose cells results in increased NMII activity and cell contractility, albeit through a Ca^{2+}-MLCK pathway.[93] Taken together, our observations contribute to the growing literature that shows βAR activation regulates force generation across a range of cell types through slightly different mechanisms; such findings suggest that βAR regulation of cellular mechanical behaviors is a convergent phenomenon that is essential to cellular homeostasis. For breast cancer cells, βAR-induced mechanotype changes are associated with altered invasive behavior, which could provide them with a selective advantage to metastasize. While we used here TNBC cell lines, future work will test how broadly this cellular response to βAR activation holds across different breast cancer subtypes, including luminal A and B, Her2, triple negative basal, and triple negative claudin-low. Future *in vivo* studies will help to elucidate the role of cellular mechanical behaviors in βAR regulation of metastasis. Ultimately a deeper understanding of the molecular signaling pathways that regulate cancer cell behaviors will advance our knowledge of cancer and benefit the rational design of more effective drugs to suppress metastasis.

Limitations of the study

The experiments presented in this study were conducted *in vitro* using established human breast cancer cell lines and an immortalized non-tumorigenic mammary epithelial cell line. Further studies using human primary tumor cells or preclinical mouse models will establish the applicability of our findings toward therapeutic applications. The chemo-mechanical model quantitatively predicts the increase in cellular traction force observed at high isoproterenol doses and qualitatively recreates other known features of cellular traction force generation on compliant versus stiff substrates, but additional validation of model predictions with targeted experiments will be required for fine-tuning model parameters and assumptions.

RESOURCE AVAILABILITY

Lead contact

Further information and request for resources, reagents, and raw data should be directed to and will be fulfilled by the lead contact, Prof. Tae-Hyung Kim (takim@salud.unm.edu).

Materials availability

The study did not generate new unique reagents and there are no restrictions to availability.

Data and code availability

- Data: This paper analyzes existing, publicly available data. The accession number for the dataset is listed in the key resources table.
- Code: The original code for Traction Force Microscopy – Pillars Assay have been deposited at GitHub: https://github.com/marvintan90/gaussianFittingForTraction. The model parameters used in computational modeling can be found in Table S1 and the Simulation source code is available at https://github.com/compactmatterlab/bAR-forces/tree/master/bAR-forces. All of these codes are publicly available as of the date of publication.
- Additional information: Any additional information required to reanalyze the data reported in this paper is available from the lead contact upon reasonable request.

ACKNOWLEDGMENTS

We thank the Flow Cytometry Core at the Broad Stem Cell Research Center at UCLA for access to the IncuCyte and flow cytometer. We also thank both the UCLA Statistical Consulting Group in the Department of Statistics and the Statistical Methods and Data Analytics Consulting Group at the Office of Advanced Research Computing at UCLA for our rigorous statistical tests. This work was supported by grants from the National Science Foundation (BMMB-1906165 and a BRITE Fellow Award CMMI-2135747 to A.C.R.; BMMB-1905390 and BMMB-1763132 to P.K.), the Army Research Office (W911NF-17-1-0413 to P.K.), the Jonsson Cancer Center Foundation, the University of California Cancer Research Coordinating Committee (CRR-18-526901 to A.C.R.), METAvivor Early Career Investigator Award to T.-H.K., and the National Institutes of Health (R21CA245667-01A1 to A.C.R., P20GM121176 and P30CA118100 to T.-H.K., and 1U54CA285117-01 to P.K.).

AUTHOR CONTRIBUTIONS

T.-H.K., M.-T.T.L., P.-Y.C., E.K.S., and A.C.R. designed the experiments. T.-H.K., M.-T.T.L., M.O., D.M.L., B.C., A.A., X.H.M.T., E.K.S., and A.C.R. performed experiments and analyzed the data. C.L. analyzed RNA-seq data. E.V.-H., C.M.F., and P.K. designed and conducted the computational modeling. E.V.-H., P.K., T.-H.K., and A.C.R. contributed to the iterative design of experiments and simulations. T.-H.K., E.K.S., P.K., and A.C.R. wrote the manuscript. All authors edited and approved the final manuscript.

DECLARATION OF INTERESTS

The authors declares no competing interests.

DECLARATION OF GENERATIVE AI AND AI-ASSISTED TECHNOLOGIES IN THE WRITING PROCESS

During the preparation of this work, the author(s) used ChatGPT in order to reduce the word count of the summary. After using this tool/service, the author(s) reviewed and edited the content as needed and take(s) full responsibility for the content of the published article.

STAR★METHODS

Detailed methods are provided in the online version of this paper and include the following:

- KEY RESOURCES TABLE
- EXPERIMENTAL MODEL AND STUDY PARTICIPANT DETAILS
  - Cell lines and reagents
- METHOD DETAILS
  - Transfections
  - Parallel microfiltration
  - Real-time qPCR
  - Western blotting
  - Traction force microscopy – Pillars Assay
  - Traction force microscopy – Beads Assay
  - Three-dimensional (3D) scratch wound invasion assay
  - Viability and apoptosis assays
  - RNA-seq analysis
  - Computational modeling
- QUANTIFICATION AND STATISTICAL ANALYSIS
  - Statistical analyses

SUPPLEMENTAL INFORMATION

Supplemental information can be found online at https://doi.org/10.1016/j.isci.2025.112676.

Received: July 19, 2022
Revised: August 6, 2024
Accepted: May 13, 2025
Published: May 15, 2025

REFERENCES

1. Wirtz, D., Konstantopoulos, K., and Searson, P.C. (2011). The physics of cancer: the role of physical interactions and mechanical forces in metastasis. Nat. Rev. Cancer *11*, 512–522. https://doi.org/10.1038/nrc3080.
2. Kraning-Rush, C.M., Califano, J.P., and Reinhart-King, C.A. (2012). Cellular traction stresses increase with increasing metastatic potential. PLoS One *7*, e32572. https://doi.org/10.1371/journal.pone.0032572.
3. Gladilin, E., Ohse, S., Boerries, M., Busch, H., Xu, C., Schneider, M., Meister, M., and Eils, R. (2019). TGFβ-induced cytoskeletal remodeling mediates elevation of cell stiffness and invasiveness in NSCLC. Sci. Rep. *9*, 7667. https://doi.org/10.1038/s41598-019-43409-x.
4. Mekhdjian, A.H., Kai, F., Rubashkin, M.G., Prahl, L.S., Przybyla, L.M., McGregor, A.L., Bell, E.S., Barnes, J.M., DuFort, C.C., Ou, G., et al. (2017). Integrin-mediated traction force enhances paxillin molecular associations and adhesion dynamics that increase the invasiveness of tumor cells into a three-dimensional extracellular matrix. Mol. Biol. Cell *28*, 1467–1488. https://doi.org/10.1091/mbc.E16-09-0654.
5. Janmey, P.A., and Miller, R.T. (2011). Mechanisms of mechanical signaling in development and disease. J. Cell Sci. *124*, 9–18. https://doi.org/10.1242/jcs.071001.
6. Petridou, N.I., Spiró, Z., and Heisenberg, C.-P. (2017). Multiscale force sensing in development. Nat. Cell Biol. *19*, 581–588. https://doi.org/10.1038/ncb3524.
7. Nardone, G., Oliver-De La Cruz, J., Vrbsky, J., Martini, C., Pribyl, J., Skládal, P., Pešl, M., Caluori, G., Pagliari, S., Martino, F., et al. (2017). YAP regulates cell mechanics by controlling focal adhesion assembly. Nat. Commun. *8*, 15321. https://doi.org/10.1038/ncomms15321.
8. Grasset, E.M., Bertero, T., Bozec, A., Friard, J., Bourget, I., Pisano, S., Lecacheur, M., Maiel, M., Bailleux, C., Emelyanov, A., et al. (2018). Matrix stiffening and EGFR cooperate to promote the collective invasion of cancer cells. Cancer Res. *78*, 5229–5242. https://doi.org/10.1158/0008-5472.CAN-18-0601.
9. Ingallina, E., Sorrentino, G., Bertolio, R., Lisek, K., Zannini, A., Azzolin, L., Severino, L.U., Scaini, D., Mano, M., Mantovani, F., et al. (2018). Mechanical cues control mutant p53 stability through a mevalonate-RhoA axis. Nat. Cell Biol. *20*, 28–35. https://doi.org/10.1038/s41556-017-0009-8.
10. Azadi, S., Tafazzoli-Shadpour, M., Soleimani, M., and Warkiani, M.E. (2019). Modulating cancer cell mechanics and actin cytoskeleton structure by chemical and mechanical stimulations. J. Biomed. Mater. Res. *107*, 1569–1581. https://doi.org/10.1002/jbm.a.36670.
11. Oh, M., Batty, S., Banerjee, N., and Kim, T.-H. (2023). High extracellular glucose promotes cell motility by modulating cell deformability and contractility via the cAMP-RhoA-ROCK axis in human breast cancer cells. Mol. Biol. Cell *34*, ar79. https://doi.org/10.1091/mbc.E22-12-0560.
12. Braadland, P.R., Ramberg, H., Grytli, H.H., and Taskén, K.A. (2014). β-Adrenergic Receptor Signaling in Prostate Cancer. Front. Oncol. *4*, 375. https://doi.org/10.3389/fonc.2014.00375.
13. Qin, J.f., Jin, F.j., Li, N., Guan, H.t., Lan, L., Ni, H., and Wang, Y. (2015). Adrenergic receptor β2 activation by stress promotes breast cancer progression through macrophages M2 polarization in tumor microenvironment. BMB Rep. *48*, 295–300. https://doi.org/10.5483/BMBRep.2015.48.5.008.
14. Wan, C., Gong, C., Zhang, H., Hua, L., Li, X., Chen, X., Chen, Y., Ding, X., He, S., Cao, W., et al. (2016). β2-adrenergic receptor signaling promotes pancreatic ductal adenocarcinoma (PDAC) progression through facilitating PCBP2-dependent c-myc expression. Cancer Lett. *373*, 67–76. https://doi.org/10.1016/j.canlet.2016.01.026.
15. Kim, T.-H., Gill, N.K., Nyberg, K.D., Nguyen, A.V., Hohlbauch, S.V., Geisse, N.A., Nowell, C.J., Sloan, E.K., and Rowat, A.C. (2016). Cancer cells become less deformable and more invasive with activation of β-adrenergic signaling. J. Cell Sci. *129*, 4563–4575. https://doi.org/10.1242/jcs.194803.
16. Sloan, E.K., Priceman, S.J., Cox, B.F., Yu, S., Pimentel, M.A., Tangkanangnukul, V., Arevalo, J.M.G., Morizono, K., Karanikolas, B.D.W., Wu, L., et al. (2010). The sympathetic nervous system induces a metastatic switch in primary breast cancer. Cancer Res. *70*, 7042–7052. https://doi.org/10.1158/0008-5472.CAN-10-0522.
17. Creed, S.J., Le, C.P., Hassan, M., Pon, C.K., Albold, S., Chan, K.T., Berginski, M.E., Huang, Z., Bear, J.E., Lane, J.R., et al. (2015). β2-adrenoceptor signaling regulates invadopodia formation to enhance tumor cell invasion. Breast Cancer Res. *17*, 145. https://doi.org/10.1186/s13058-015-0655-3.
18. Le, C.P., Nowell, C.J., Kim-Fuchs, C., Botteri, E., Hiller, J.G., Ismail, H., Pimentel, M.A., Chai, M.G., Karnezis, T., Rotmensz, N., et al. (2016). Chronic stress in mice remodels lymph vasculature to promote tumour cell dissemination. Nat. Commun. *7*, 10634. https://doi.org/10.1038/ncomms10634.
19. Hiller, J.G., Cole, S.W., Crone, E.M., Byrne, D.J., Shackleford, D.M., Pang, J.-M.B., Henderson, M.A., Nightingale, S.S., Ho, K.M., Myles, P. S., et al. (2020). Preoperative β-Blockade with Propranolol Reduces Biomarkers of Metastasis in Breast Cancer: A Phase II Randomized Trial. Clin. Cancer Res. *26*, 1803–1811. https://doi.org/10.1158/1078-0432.CCR-19-2641.
20. Shaashua, L., Shabat-Simon, M., Haldar, R., Matzner, P., Zmora, O., Shabtai, M., Sharon, E., Allweis, T., Barshack, I., Hayman, L., et al. (2017). Perioperative COX-2 and β-Adrenergic Blockade Improves Metastatic Biomarkers in Breast Cancer Patients in a Phase-II Randomized

Trial. Clin. Cancer Res. *23*, 4651–4661. https://doi.org/10.1158/1078-0432.CCR-17-0152.

21. De Giorgi, V., Grazzini, M., Benemei, S., Marchionni, N., Botteri, E., Pennacchioli, E., Geppetti, P., and Gandini, S. (2018). Propranolol for Off-label Treatment of Patients With Melanoma: Results From a Cohort Study. JAMA Oncol. *4*, e172908. https://doi.org/10.1001/jamaoncol.2017.2908.
22. Powe, D.G., Voss, M.J., Zänker, K.S., Habashy, H.O., Green, A.R., Ellis, I. O., and Entschladen, F. (2010). Beta-blocker drug therapy reduces secondary cancer formation in breast cancer and improves cancer specific survival. Oncotarget *1*, 628–638. https://doi.org/10.18632/oncotarget.101009.
23. Barron, T.I., Connolly, R.M., Sharp, L., Bennett, K., and Visvanathan, K. (2011). Beta blockers and breast cancer mortality: a population- based study. J. Clin. Oncol. *29*, 2635–2644. https://doi.org/10.1200/JCO.2010.33.5422.
24. Melhem-Bertrandt, A., Chavez-Macgregor, M., Lei, X., Brown, E.N., Lee, R.T., Meric-Bernstam, F., Sood, A.K., Conzen, S.D., Hortobagyi, G.N., and Gonzalez-Angulo, A.-M. (2011). Beta-blocker use is associated with improved relapse-free survival in patients with triple-negative breast cancer. J. Clin. Oncol. *29*, 2645–2652. https://doi.org/10.1200/JCO.2010.33.4441.
25. Scott, O.W., Tin Tin, S., Elwood, J.M., Cavadino, A., Habel, L.A., Kuper-Hommel, M., Campbell, I., and Lawrenson, R. (2022). Post-diagnostic beta blocker use and breast cancer-specific mortality: a population-based cohort study. Breast Cancer Res. Treat. *193*, 225–235. https://doi.org/10.1007/s10549-022-06528-0.
26. Løfling, L.L., Støer, N.C., Sloan, E.K., Chang, A., Gandini, S., Ursin, G., and Botteri, E. (2022). β-blockers and breast cancer survival by molecular subtypes: a population-based cohort study and meta-analysis. Br. J. Cancer *127*, 1086–1096. https://doi.org/10.1038/s41416-022-01891-7.
27. Motomura, S., Reinhard-Zerkowski, H., Daul, A., and Brodde, O.E. (1990). On the physiologic role of beta-2 adrenoceptors in the human heart: in vitro and in vivo studies. Am. Heart J. *119*, 608–619. https://doi.org/10.1016/s0002-8703(05)80284-4.
28. Goldie, R.G., Spina, D., Henry, P.J., Lulich, K.M., and Paterson, J.W. (1986). In vitro responsiveness of human asthmatic bronchus to carbachol, histamine, beta-adrenoceptor agonists and theophylline. Br. J. Clin. Pharmacol. *22*, 669–676. https://doi.org/10.1111/j.1365-2125.1986.tb02956.x.
29. Spurzem, J.R., Gupta, J., Veys, T., Kneifl, K.R., Rennard, S.I., and Wyatt, T.A. (2002). Activation of protein kinase A accelerates bovine bronchial epithelial cell migration. Am. J. Physiol. Lung Cell. Mol. Physiol. *282*, L1108–L1116. https://doi.org/10.1152/ajplung.00148.2001.
30. Steenhuis, P., Huntley, R.E., Gurenko, Z., Yin, L., Dale, B.A., Fazel, N., and Isseroff, R.R. (2011). Adrenergic signaling in human oral keratinocytes and wound repair. J. Dent. Res. *90*, 186–192. https://doi.org/10.1177/0022034510388034.
31. Pullar, C.E., Zhao, M., Song, B., Pu, J., Reid, B., Ghoghawala, S., McCaig, C., and Isseroff, R.R. (2007). Beta-adrenergic receptor agonists delay while antagonists accelerate epithelial wound healing: evidence of an endogenous adrenergic network within the corneal epithelium. J. Cell. Physiol. *211*, 261–272. https://doi.org/10.1002/jcp.20934.
32. Ghoghawala, S.Y., Mannis, M.J., Pullar, C.E., Rosenblatt, M.I., and Isseroff, R.R. (2008). Beta2-adrenergic receptor signaling mediates corneal epithelial wound repair. Investig. Ophthalmol. Vis. Sci. *49*, 1857–1863. https://doi.org/10.1167/iovs.07-0925.
33. He, Y., Yu, Z., Ge, D., Wang-Sattler, R., Thiesen, H.-J., Xie, L., and Li, Y. (2012). Cell type specificity of signaling: view from membrane receptors distribution and their downstream transduction networks. Protein Cell *3*, 701–713. https://doi.org/10.1007/s13238-012-2049-y.
34. Pon, C.K., Lane, J.R., Sloan, E.K., and Halls, M.L. (2016). The β2-adrenoceptor activates a positive cAMP-calcium feedforward loop to drive breast cancer cell invasion. FASEB J. *30*, 1144–1154. https://doi.org/10.1096/fj.15-277798.
35. Ma, X., Zhao, Y., Daaka, Y., and Nie, Z. (2012). Acute activation of β2-adrenergic receptor regulates focal adhesions through βArrestin2- and p115RhoGEF protein-mediated activation of RhoA. J. Biol. Chem. *287*, 18925–18936. https://doi.org/10.1074/jbc.M112.352260.
36. Fogli, S., Stefanelli, F., Battolla, B., Bianchi, F., Breschi, M.C., and Mattii, L. (2015). Salbutamol inhibits RhoA activation in normal but not in desensitized bronchial smooth muscle cells. J. Pharm. Pharmacol. *67*, 1416–1420. https://doi.org/10.1111/jphp.12444.
37. Delmotte, P., Ressmeyer, A.-R., Bai, Y., and Sanderson, M.J. (2010). Mechanisms of airway smooth muscle relaxation induced by beta2-adrenergic agonists. Front. Biosci. (Landmark Ed) *15*, 750–764. https://doi.org/10.2741/3644.
38. Moore, R.H., Tuffaha, A., Millman, E.E., Dai, W., Hall, H.S., Dickey, B.F., and Knoll, B.J. (1999). Agonist-induced sorting of human beta2-adrenergic receptors to lysosomes during downregulation. J. Cell Sci. *112*, 329–338. https://doi.org/10.1242/jcs.112.3.329.
39. Vicente-Manzanares, M., Ma, X., Adelstein, R.S., and Horwitz, A.R. (2009). Non-muscle myosin II takes centre stage in cell adhesion and migration. Nat. Rev. Mol. Cell Biol. *10*, 778–790. https://doi.org/10.1038/nrm2786.
40. Aguilar-Cuenca, R., Llorente-González, C., Chapman, J.R., Talayero, V. C., Garrido-Casado, M., Delgado-Arévalo, C., Millán-Salanova, M., Shabanowitz, J., Hunt, D.F., Sellers, J.R., et al. (2020). Tyrosine Phosphorylation of the Myosin Regulatory Light Chain Controls Non-muscle Myosin II Assembly and Function in Migrating Cells. Curr. Biol. *30*, 2446–2458.e6. https://doi.org/10.1016/j.cub.2020.04.057.
41. Messier, T.L., Gordon, J.A.R., Boyd, J.R., Tye, C.E., Browne, G., Stein, J. L., Lian, J.B., and Stein, G.S. (2016). Histone H3 lysine 4 acetylation and methylation dynamics define breast cancer subtypes. Oncotarget *7*, 5094–5109. https://doi.org/10.18632/oncotarget.6922.
42. Qi, D., Kaur Gill, N., Santiskulvong, C., Sifuentes, J., Dorigo, O., Rao, J., Taylor-Harding, B., Ruprecht Wiedemeyer, W., and Rowat, A.C. (2015). Screening cell mechanotype by parallel microfiltration. Sci. Rep. *5*, 17595. https://doi.org/10.1038/srep17595.
43. Gargiulo, L., Copsel, S., Rivero, E.M., Galés, C., Sénard, J.-M., Lüthy, I. A., Davio, C., and Bruzzone, A. (2014). Differential β_2-adrenergic receptor expression defines the phenotype of non-tumorigenic and malignant human breast cell lines. Oncotarget *5*, 10058–10069. https://doi.org/10.18632/oncotarget.2460.
44. Vazquez-Hidalgo, E., Farris, C.M., Rowat, A.C., and Katira, P. (2022). Chemo-Mechanical Factors That Limit Cellular Force Generation. Front. Phys. *10*. https://doi.org/10.3389/fphy.2022.831776.
45. Califano, J.P., and Reinhart-King, C.A. (2010). Substrate stiffness and cell area predict cellular traction stresses in single cells and cells in contact. Cell. Mol. Bioeng. *3*, 68–75. https://doi.org/10.1007/s12195-010-0102-6.
46. Han, S.J., Bielawski, K.S., Ting, L.H., Rodriguez, M.L., and Sniadecki, N. J. (2012). Decoupling substrate stiffness, spread area, and micropost density: a close spatial relationship between traction forces and focal adhesions. Biophys. J. *103*, 640–648. https://doi.org/10.1016/j.bpj.2012.07.023.
47. Stam, S., Alberts, J., Gardel, M.L., and Munro, E. (2015). Isoforms confer characteristic force generation and mechanosensation by myosin II filaments. Biophys. J. *108*, 1997–2006. https://doi.org/10.1016/j.bpj.2015.03.030.
48. Marzban, B., Yi, X., and Yuan, H. (2018). A minimal mechanics model for mechanosensing of substrate rigidity gradient in durotaxis. Biomech. Model. Mechanobiol. *17*, 915–922. https://doi.org/10.1007/s10237-018-1001-3.
49. Yeoman, B.M., and Katira, P. (2018). A stochastic algorithm for accurately predicting path persistence of cells migrating in 3D matrix environments. PLoS One *13*, e0207216. https://doi.org/10.1371/journal.pone.0207216.

50. Tamura, M., Nakao, H., Yoshizaki, H., Shiratsuchi, M., Shigyo, H., Yamada, H., Ozawa, T., Totsuka, J., and Hidaka, H. (2005). Development of specific Rho-kinase inhibitors and their clinical application. Biochim. Biophys. Acta *1754*, 245–252. https://doi.org/10.1016/j.bbapap.2005.06.015.

51. Lam, W.A., Rosenbluth, M.J., and Fletcher, D.A. (2007). Chemotherapy exposure increases leukemia cell stiffness. Blood *109*, 3505–3508. https://doi.org/10.1182/blood-2006-08-043570.

52. Maekawa, M., Ishizaki, T., Boku, S., Watanabe, N., Fujita, A., Iwamatsu, A., Obinata, T., Ohashi, K., Mizuno, K., and Narumiya, S. (1999). Signaling from Rho to the actin cytoskeleton through protein kinases ROCK and LIM-kinase. Science *285*, 895–898. https://doi.org/10.1126/science.285.5429.895.

53. Watanabe, N., Kato, T., Fujita, A., Ishizaki, T., and Narumiya, S. (1999). Cooperation between mDia1 and ROCK in Rho-induced actin reorganization. Nat. Cell Biol. *1*, 136–143. https://doi.org/10.1038/11056.

54. Swaminathan, V., Mythreye, K., O'Brien, E.T., Berchuck, A., Blobe, G.C., and Superfine, R. (2011). Mechanical stiffness grades metastatic potential in patient tumor cells and in cancer cell lines. Cancer Res. *71*, 5075–5080. https://doi.org/10.1158/0008-5472.CAN-11-0247.

55. Xu, W., Mezencev, R., Kim, B., Wang, L., McDonald, J., and Sulchek, T. (2012). Cell stiffness is a biomarker of the metastatic potential of ovarian cancer cells. PLoS One *7*, e46609. https://doi.org/10.1371/journal.pone.0046609.

56. Nyberg, K.D., Bruce, S.L., Nguyen, A.V., Chan, C.K., Gill, N.K., Kim, T.-H., Sloan, E.K., and Rowat, A.C. (2018). Predicting cancer cell invasion by single-cell physical phenotyping. Integr. Biol. *10*, 218–231. https://doi.org/10.1039/c7ib00222j.

57. Pan, Y., Robertson, G., Pedersen, L., Lim, E., Hernandez-Herrera, A., Rowat, A.C., Patil, S.L., Chan, C.K., Wen, Y., Zhang, X., et al. (2016). miR-509-3p is clinically significant and strongly attenuates cellular migration and multi-cellular spheroids in ovarian cancer. Oncotarget *7*, 25930–25948. https://doi.org/10.18632/oncotarget.8412.

58. Kothari, P., Johnson, C., Sandone, C., Iglesias, P.A., and Robinson, D.N. (2019). How the mechanobiome drives cell behavior, viewed through the lens of control theory. J. Cell Sci. *132*, jcs234476. https://doi.org/10.1242/jcs.234476.

59. Wolfenson, H., Yang, B., and Sheetz, M.P. (2019). Steps in Mechanotransduction Pathways that Control Cell Morphology. Annu. Rev. Physiol. *81*, 585–605. https://doi.org/10.1146/annurev-physiol-021317-121245.

60. Perdrix Rosell, A., Maiques, O., Martin, J.A.J., Chakravarty, P., Ombrato, L., Sanz-Moreno, V., and Malanchi, I. (2022). Early functional mismatch between breast cancer cells and their tumour microenvironment suppresses long term growth. Cancer Lett. *544*, 215800. https://doi.org/10.1016/j.canlet.2022.215800.

61. Moose, D.L., Krog, B.L., Kim, T.-H., Zhao, L., Williams-Perez, S., Burke, G., Rhodes, L., Vanneste, M., Breheny, P., Milhem, M., et al. (2020). Cancer Cells Resist Mechanical Destruction in Circulation via RhoA/Actomyosin-Dependent Mechano-Adaptation. Cell Rep. *30*, 3864–3874.e6. https://doi.org/10.1016/j.celrep.2020.02.080.

62. Peng, Y., Chen, Z., Chen, Y., Li, S., Jiang, Y., Yang, H., Wu, C., You, F., Zheng, C., Zhu, J., et al. (2019). ROCK isoforms differentially modulate cancer cell motility by mechanosensing the substrate stiffness. Acta Biomater. *88*, 86–101. https://doi.org/10.1016/j.actbio.2019.02.015.

63. Vennin, C., Chin, V.T., Warren, S.C., Lucas, M.C., Herrmann, D., Magenau, A., Melenec, P., Walters, S.N., del Monte-Nieto, G., Conway, J.R.W., et al. (2017). Transient tissue priming via ROCK inhibition uncouples pancreatic cancer progression, sensitivity to chemotherapy, and metastasis. Sci. Transl. Med. *9*, eaai8504. https://doi.org/10.1126/scitranslmed.aai8504.

64. Daubriac, J., Han, S., Grahovac, J., Smith, E., Hosein, A., Buchanan, M., Basik, M., and Boucher, Y. (2018). The crosstalk between breast carcinoma-associated fibroblasts and cancer cells promotes RhoA-dependent invasion via IGF-1 and PAI-1. Oncotarget *9*, 10375–10387. https://doi.org/10.18632/oncotarget.23735.

65. Sood, A.K., Armaiz-Pena, G.N., Halder, J., Nick, A.M., Stone, R.L., Hu, W., Carroll, A.R., Spannuth, W.A., Deavers, M.T., Allen, J.K., et al. (2010). Adrenergic modulation of focal adhesion kinase protects human ovarian cancer cells from anoikis. J. Clin. Investig. *120*, 1515–1523. https://doi.org/10.1172/JCI40802.

66. Meyer, T., Marshall, J.F., and Hart, I.R. (1998). Expression of alphav integrins and vitronectin receptor identity in breast cancer cells. Br. J. Cancer *77*, 530–536. https://doi.org/10.1038/bjc.1998.86.

67. Schwartz, A.D., Hall, C.L., Barney, L.E., Babbitt, C.C., and Peyton, S.R. (2018). Integrin α6 and EGFR signaling converge at mechanosensitive calpain 2. Biomaterials *178*, 73–82. https://doi.org/10.1016/j.biomaterials.2018.05.056.

68. Jonas, O., Mierke, C.T., and Käs, J.A. (2011). Invasive cancer cell lines exhibit biomechanical properties that are distinct from their noninvasive counterparts. Soft Matter *7*, 11488. https://doi.org/10.1039/c1sm05532a.

69. Ali, M.R.K., Wu, Y., Ghosh, D., Do, B.H., Chen, K., Dawson, M.R., Fang, N., Sulchek, T.A., and El-Sayed, M.A. (2017). Nuclear Membrane-Targeted Gold Nanoparticles Inhibit Cancer Cell Migration and Invasion. ACS Nano *11*, 3716–3726. https://doi.org/10.1021/acsnano.6b08345.

70. Wottawah, F., Schinkinger, S., Lincoln, B., Ebert, S., Müller, K., Sauer, F., Travis, K., and Guck, J. (2005). Characterizing single suspended cells by optorheology. Acta Biomater. *1*, 263–271. https://doi.org/10.1016/j.actbio.2005.02.010.

71. Guck, J., Schinkinger, S., Lincoln, B., Wottawah, F., Ebert, S., Romeyke, M., Lenz, D., Erickson, H.M., Ananthakrishnan, R., Mitchell, D., et al. (2005). Optical deformability as an inherent cell marker for testing malignant transformation and metastatic competence. Biophys. J. *88*, 3689–3698. https://doi.org/10.1529/biophysj.104.045476.

72. Yubero, M.L., Kosaka, P.M., San Paulo, Á., Malumbres, M., Calleja, M., and Tamayo, J. (2020). Effects of energy metabolism on the mechanical properties of breast cancer cells. Commun. Biol. *3*, 590. https://doi.org/10.1038/s42003-020-01330-4.

73. Murphy, D.A., and Courtneidge, S.A. (2011). The "ins" and "outs" of podosomes and invadopodia: characteristics, formation and function. Nat. Rev. Mol. Cell Biol. *12*, 413–426. https://doi.org/10.1038/nrm3141.

74. Nürnberg, A., Kitzing, T., and Grosse, R. (2011). Nucleating actin for invasion. Nat. Rev. Cancer *11*, 177–187. https://doi.org/10.1038/nrc3003.

75. Liu, Y.-J., Le Berre, M., Lautenschlaeger, F., Maiuri, P., Callan-Jones, A., Heuzé, M., Takaki, T., Voituriez, R., and Piel, M. (2015). Confinement and low adhesion induce fast amoeboid migration of slow mesenchymal cells. Cell *160*, 659–672. https://doi.org/10.1016/j.cell.2015.01.007.

76. Barbier, L., Sáez, P.J., Attia, R., Lennon-Duménil, A.-M., Lavi, I., Piel, M., and Vargas, P. (2019). Myosin II activity is selectively needed for migration in highly confined microenvironments in mature dendritic cells. Front. Immunol. *10*, 747. https://doi.org/10.3389/fimmu.2019.00747.

77. Nguyen, A.V., Trompetto, B., Tan, X.H.M., Scott, M.B., Hu, K.H.H., Deeds, E., Butte, M.J., Chiou, P.Y., and Rowat, A.C. (2020). Differential contributions of actin and myosin to the physical phenotypes and invasion of pancreatic cancer cells. Cell. Mol. Bioeng. *13*, 27–44. https://doi.org/10.1007/s12195-019-00603-1.

78. Kazazian, K., Go, C., Wu, H., Brashavitskaya, O., Xu, R., Dennis, J.W., Gingras, A.-C., and Swallow, C.J. (2017). Plk4 Promotes Cancer Invasion and Metastasis through Arp2/3 Complex Regulation of the Actin Cytoskeleton. Cancer Res. *77*, 434–447. https://doi.org/10.1158/0008-5472.CAN-16-2060.

79. Munshi, H.G., and Stack, M.S. (2006). Reciprocal interactions between adhesion receptor signaling and MMP regulation. Cancer Metastasis Rev. *25*, 45–56. https://doi.org/10.1007/s10555-006-7888-7.

80. Minneman, K.P., Pittman, R.N., and Molinoff, P.B. (1981). Beta-adrenergic receptor subtypes: properties, distribution, and regulation. Annu. Rev. Neurosci. *4*, 419–461. https://doi.org/10.1146/annurev.ne.04.030181.002223.

81. Mak, J.C., Nishikawa, M., Haddad, E.B., Kwon, O.J., Hirst, S.J., Twort, C. H., and Barnes, P.J. (1996). Localisation and expression of beta-adrenoceptor subtype mRNAs in human lung. Eur. J. Pharmacol. *302*, 215–221. https://doi.org/10.1016/0014-2999(96)00104-5.

82. Bruzzone, A., Saulière, A., Finana, F., Sénard, J.-M., Lüthy, I., and Galés, C. (2014). Dosage-dependent regulation of cell proliferation and adhesion through dual β2-adrenergic receptor/cAMP signals. FASEB J. *28*, 1342–1354. https://doi.org/10.1096/fj.13-239285.

83. Milligan, G., Svoboda, P., and Brown, C.M. (1994). Why are there so many adrenoceptor subtypes? Biochem. Pharmacol. *48*, 1059–1071. https://doi.org/10.1016/0006-2952(94)90141-4.

84. Barnes, W.G., Reiter, E., Violin, J.D., Ren, X.-R., Milligan, G., and Lefkowitz, R.J. (2005). beta-Arrestin 1 and Galphaq/11 coordinately activate RhoA and stress fiber formation following receptor stimulation. J. Biol. Chem. *280*, 8041–8050. https://doi.org/10.1074/jbc.M412924200.

85. Reiter, E., and Lefkowitz, R.J. (2006). GRKs and beta-arrestins: roles in receptor silencing, trafficking and signaling. Trends Endocrinol. Metab. *17*, 159–165. https://doi.org/10.1016/j.tem.2006.03.008.

86. Carr, R., Schilling, J., Song, J., Carter, R.L., Du, Y., Yoo, S.M., Traynham, C.J., Koch, W.J., Cheung, J.Y., Tilley, D.G., and Benovic, J.L. (2016). β--arrestin-biased signaling through the β2-adrenergic receptor promotes cardiomyocyte contraction. Proc. Natl. Acad. Sci. USA *113*, E4107–E4116. https://doi.org/10.1073/pnas.1606267113.

87. Luttrell, L.M., Ferguson, S.S., Daaka, Y., Miller, W.E., Maudsley, S., Della Rocca, G.J., Lin, F., Kawakatsu, H., Owada, K., Luttrell, D.K., et al. (1999). Beta-arrestin-dependent formation of beta2 adrenergic receptor-Src protein kinase complexes. Science *283*, 655–661. https://doi.org/10.1126/science.283.5402.655.

88. Armaiz-Pena, G.N., Allen, J.K., Cruz, A., Stone, R.L., Nick, A.M., Lin, Y. G., Han, L.Y., Mangala, L.S., Villares, G.J., Vivas-Mejia, P., et al. (2013). Src activation by β-adrenoreceptors is a key switch for tumour metastasis. Nat. Commun. *4*, 1403. https://doi.org/10.1038/ncomms2413.

89. He, Q., Wu, G., and Lapointe, M.C. (2000). Isoproterenol and cAMP regulation of the human brain natriuretic peptide gene involves Src and Rac. Am. J. Physiol. Endocrinol. Metab. *278*, E1115–E1123. https://doi.org/10.1152/ajpendo.2000.278.6.E1115.

90. Barbieri, A., Bimonte, S., Palma, G., Luciano, A., Rea, D., Giudice, A., Scognamiglio, G., La Mantia, E., Franco, R., Perdonà, S., et al. (2015). The stress hormone norepinephrine increases migration of prostate cancer cells in vitro and in vivo. Int. J. Oncol. *47*, 527–534. https://doi.org/10.3892/ijo.2015.3038.

91. Ribeiro, A.J.S., Schwab, O., Mandegar, M.A., Ang, Y.-S., Conklin, B.R., Srivastava, D., and Pruitt, B.L. (2017). Multi-Imaging Method to Assay the Contractile Mechanical Output of Micropatterned Human iPSC-Derived Cardiac Myocytes. Circ. Res. *120*, 1572–1583. https://doi.org/10.1161/CIRCRESAHA.116.310363.

92. Wang, N., Tolić-Nørrelykke, I.M., Chen, J., Mijailovich, S.M., Butler, J.P., Fredberg, J.J., and Stamenović, D. (2002). Cell prestress. I. Stiffness and prestress are closely associated in adherent contractile cells. Am. J. Physiol. Cell Physiol. *282*, C606–C616. https://doi.org/10.1152/ajpcell.00269.2001.

93. Tharp, K.M., Kang, M.S., Timblin, G.A., Dempersmier, J., Dempsey, G.E., Zushin, P.-J.H., Benavides, J., Choi, C., Li, C.X., Jha, A.K., et al. (2018). Actomyosin-Mediated Tension Orchestrates Uncoupled Respiration in Adipose Tissues. Cell Metab. *27*, 602–615.e4. https://doi.org/10.1016/j.cmet.2018.02.005.

94. Le, C.P., Karnezis, T., Achen, M.G., Stacker, S.A., and Sloan, E.K. (2013). Lymphovascular and neural regulation of metastasis: shared tumour signalling pathways and novel therapeutic approaches. Best Pract. Res. Clin. Anaesthesiol. *27*, 409–425. https://doi.org/10.1016/j.bpa.2013.10.008.

95. Chang, A., Le, C.P., Walker, A.K., Creed, S.J., Pon, C.K., Albold, S., Carroll, D., Halls, M.L., Lane, J.R., Riedel, B., et al. (2016). β2-Adrenoceptors on tumor cells play a critical role in stress-enhanced metastasis in a mouse model of breast cancer. Brain Behav. Immun. *57*, 106–115. https://doi.org/10.1016/j.bbi.2016.06.011.

96. Pillé, J.Y., Denoyelle, C., Varet, J., Bertrand, J.R., Soria, J., Opolon, P., Lu, H., Pritchard, L.L., Vannier, J.P., Malvy, C., et al. (2005). Anti-RhoA and anti-RhoC siRNAs inhibit the proliferation and invasiveness of MDA-MB-231 breast cancer cells in vitro and in vivo. Mol. Ther. *11*, 267–274. https://doi.org/10.1016/j.ymthe.2004.08.029.

97. Gill, N.K., Gill, N.K., Qi, D., Kim, T.-H., Chan, C., Nguyen, A., Nyberg, K. D., and Rowat, A.C. (2017). A protocol for screening cells based on deformability using parallel microfiltration. Protoc. Exch. https://doi.org/10.1038/protex.2017.101.

98. Gill, N.K., Ly, C., Nyberg, K.D., Lee, L., Qi, D., Tofig, B., Reis-Sobreiro, M., Dorigo, O., Rao, J., Wiedemeyer, R., et al. (2019). A scalable filtration method for high throughput screening based on cell deformability. Lab Chip *19*, 343–357. https://doi.org/10.1039/c8lc00922h.

99. Xiao, F., Wen, X., Tan, X.H.M., and Chiou, P.-Y. (2018). Plasmonic micropillars for precision cell force measurement across a large field-of-view. Appl. Phys. Lett. *112*, 033701. https://doi.org/10.1063/1.5005525.

100. Yokota, T., McCourt, J., Ma, F., Ren, S., Li, S., Kim, T.-H., Kurmangaliyev, Y.Z., Nasiri, R., Ahadian, S., Nguyen, T., et al. (2020). Type V Collagen in Scar Tissue Regulates the Size of Scar after Heart Injury. Cell *182*, 545–562.e23. https://doi.org/10.1016/j.cell.2020.06.030.

101. Martiel, J.-L., Leal, A., Kurzawa, L., Balland, M., Wang, I., Vignaud, T., Tseng, Q., and Théry, M. (2015). Measurement of cell traction forces with ImageJ. Methods Cell Biol. *125*, 269–287. https://doi.org/10.1016/bs.mcb.2014.10.008.

102. Huxley, A.F. (1974). Muscular contraction. J. Physiol. (Lond.) *243*, 1–43.

103. Spudich, J.A. (2001). The myosin swinging cross-bridge model. Nat. Rev. Mol. Cell Biol. *2*, 387–392. https://doi.org/10.1038/35073086.

104. Williams, C.D., Regnier, M., and Daniel, T.L. (2010). Axial and radial forces of cross-bridges depend on lattice spacing. PLoS Comput. Biol. *6*, e1001018. https://doi.org/10.1371/journal.pcbi.1001018.

105. Cramer, L.P., Siebert, M., and Mitchison, T.J. (1997). Identification of novel graded polarity actin filament bundles in locomoting heart fibroblasts: implications for the generation of motile force. J. Cell Biol. *136*, 1287–1305. https://doi.org/10.1083/jcb.136.6.1287.

106. Hu, S., Tee, Y.-H., Kabla, A., Zaidel-Bar, R., Bershadsky, A., and Hersen, P. (2015). Structured illumination microscopy reveals focal adhesions are composed of linear subunits. Cytoskeleton (Hoboken) *72*, 235–245. https://doi.org/10.1002/cm.21223.

107. Young, L.E., and Higgs, H.N. (2018). Focal Adhesions Undergo Longitudinal Splitting into Fixed-Width Units. Curr. Biol. *28*, 2033–2045.e5. https://doi.org/10.1016/j.cub.2018.04.073.

108. Mak, M., Zaman, M.H., Kamm, R.D., and Kim, T. (2016). Interplay of active processes modulates tension and drives phase transition in self-renewing, motor-driven cytoskeletal networks. Nat. Commun. *7*, 10323. https://doi.org/10.1038/ncomms10323.

109. Verkhovsky, A.B., and Borisy, G.G. (1993). Non-sarcomeric mode of myosin II organization in the fibroblast lamellum. J. Cell Biol. *123*, 637–652. https://doi.org/10.1083/jcb.123.3.637.

110. Billington, N., Wang, A., Mao, J., Adelstein, R.S., and Sellers, J.R. (2013). Characterization of three full-length human nonmuscle myosin II paralogs. J. Biol. Chem. *288*, 33398–33410. https://doi.org/10.1074/jbc.M113.499848.

111. Thoresen, T., Lenz, M., and Gardel, M.L. (2013). Thick filament length and isoform composition determine self-organized contractile units in actomyosin bundles. Biophys. J. *104*, 655–665. https://doi.org/10.1016/j.bpj.2012.12.042.

112. Farris, C.M. (2017). The Role of Myosin Head State and Binding Site Availability in Calcium-Dependent Regulation of a Muscle Mimetic System. Masters Abstracts International *57*, 91.

113. Veigel, C., Molloy, J.E., Schmitz, S., and Kendrick-Jones, J. (2003). Load-dependent kinetics of force production by smooth muscle myosin measured with optical tweezers. Nat. Cell Biol. *5*, 980–986. https://doi.org/10.1038/ncb1060.

CellPress
OPEN ACCESS

STAR★METHODS

KEY RESOURCES TABLE

REAGENT or RESOURCE	SOURCE	IDENTIFIER
Antibodies		
GAPDH	ThermoFisher	Cat# MA5-15738
Phospho-MLC2 (Ser 19)	Cell Signaling Technology	Cat# 3671
Phospho-MLC2 (Thr18/Ser19)	Cell Signaling Technology	Cat# 3674
Total MLC2	Sigma	Cat# M4401
RhoA	ThermoFisher	Cat# MA1-134
Chemicals, peptides, and recombinant proteins		
(−)-Isoproterenol hydrochloride	MilliporeSigma	Cat# I6504
(±)-Propranolol hydrochloride	MilliporeSigma	Cat# P0884
Blebbistatin	Selleckchem	Cat# S7099
Y27632 dihydrochloride	Selleckchem	Cat# S1049
Glycyl-H 1152 dihydrochloride	Tocris	Cat# 24-851
ML-7 hydrochloride	Selleckchem	Cat# S8388
IPA-3	Selleckchem	Cat# S7093
Rho Activator II	Cytoskeleton	Cat# CN03-A
Critical commercial assays		
Lipofectamine 3000 Transfection	ThermoFisher	Cat# L3000008
Pierce™ BCA Protein Assay Kit	ThermoFisher	Cat# 23225
Dead Cell Apoptosis Kit	ThermoFisher	Cat# V13241
Qiagen RNeasy Mini	QIAGEN	Cat# 74104
RNase-Free DNase Set	QIAGEN	Cat# 79254
QuantiTect RT-PCR Kits	QIAGEN	Cat# 204443
Deposited data		
RNA-seq data published by Messier et al. (Oncotarget. 2016; 7:5094-5109.)	NCBI GEO	GSE69377
Experimental models: Cell lines		
MDA-MB-468	ATCC	NCI-60 Human Tumor Cell Lines
MDA-MB-231^{HM}	Provided by Dr. Zhou Ou, Fudan University Shanghai Cancer Center	N/A
MCF10A	ATCC	N/A
MDA-MB-231	ATCC	NCI-60 Human Tumor Cell Lines
MCF7	ATCC	NCI-60 Human Tumor Cell Lines
Oligonucleotides		
siRhoA-#1	Millipore-Sigma	Cat# VC30002 5′-AUGGAAAGCAGGUAGAGUU-3′
siRhoA-#2	Millipore-Sigma	Cat# VC30002 5′-GAAAGACAUGCUUGCUCAU-3′
siControl	Millipore-Sigma	Cat# VC30002 5′-CAGUCAGGAGGAUCCAAAGTG-3′
Primer-probes for human ADRB2	ThermoFisher	Hs00240532_s1
Primer-probes for human GAPDH	ThermoFisher	Hs02758991_g1
Software and algorithms		
GraphPad Prism 10	GraphPad Software	N/A
MATLAB	The MathWorks, Inc.	Source code is available at https://github.com/marvintan90/gaussianFittingForTraction

(*Continued on next page*)

Continued

REAGENT or RESOURCE	SOURCE	IDENTIFIER
IncuCyte™ Zoom 2018A	Essen BioScience (Sartorius)	N/A
Fiji (ImageJ)	ImageJ software	https://doi.org/10.1038/nmeth.2019
CFX Manager Software v3.1	Bio-Rad	N/A

EXPERIMENTAL MODEL AND STUDY PARTICIPANT DETAILS

Cell lines and reagents

The triple-negative breast adenocarcinoma cell lines, MDA-MB-468 and a highly metastatic variant of the cell line, MDA-MB-231^{HM}, were cultured as previously described.[15,18] MDA-MB-231^{HM} is well established to mimic metastatic breast cancer in orthotopic mouse model[94] and is thus considered a robust model for *in vitro* studies of cancer cell behavior.[95] The non-tumorigenic mammary epithelial cell line (MCF10A) was cultured in DMEM/F12 media supplemented with 5% horse serum, 1% pen/strep, 20 ng/mL EGF, 0.5 μg/mL hydrocortisone, 100 ng/mL cholera toxin, and 10 μg/mL insulin. The βAR agonist, isoproterenol, and antagonist, propranolol, were from MilliporeSigma (Burlington, MA, USA). To inhibit the activity of non-muscle myosin II we used (−)-blebbistatin (Selleckchem). Rho-associated protein kinases (ROCKs) were inhibited using Y27632 dihydrochloride (Y27632, Selleckchem) and glycyl-H 1152 dihydrochloride (g-H-1152, Tocris); myosin light-chain kinase (MLCK) was inhibited using ML-7 hydrochloride (ML-7, Selleckchem); and p21 activated kinase 1 (PAK1) was inhibited using IPA-3 (Selleckchem). Cells were treated with drugs at 10 μM for 24 h prior to measurements unless stated otherwise. To activate RhoA GTPase, cells were treated with Rho Activator II (CN03, Cytoskeleton) for 4 h.

METHOD DETAILS

Transfections

siRNA transfections were performed using Lipofectamine 3000 (ThermoFisher) according to manufacturer's instructions. Briefly, 50 nM of siRNAs were diluted in reduced-serum medium (Opti-MEM, Gibco) and mixed with Lipofectamine 3000 diluted in Opti-MEM followed by incubation for 5 min at room temperature. The mixture of siRNA and transfection reagent was added to the cell culture plate dropwise and cells were incubated for 72 h prior to measurement. We used the following siRNA sequences for RhoA and scrambled control[9,96]: siRhoA-#1: 5′-AUGGAAAGCAGGUAGAGUU-3′, siRhoA-#2: 5′-GAAAGACAUGCUUGCUCAU-3′, siControl: 5′-CAGUCAGGAGGAUCCAAAGTG-3′.

Parallel microfiltration

To measure whole cell deformability, we used parallel microfiltration (PMF).[42,97] Cells were trypsinized with 0.25% trypsin-EDTA and cells in suspension were counted using an automated cell counter (TC20, Bio-Rad) and resuspended in medium to a density of 5×10^5 cells/mL. We also used the automated cell counter (TC20) to measure cell size distributions. To allow for cells to equilibrate after lifting into suspension, suspensions were maintained for 30 min prior to filtration. To drive cells through the 10 μm pores of the polycarbonate membrane (Millipore), we applied air pressure (2.0 kPa) for 20 s. To quantify the magnitude of cell filtration, we determined the volume of media that remained in the top well after filtration by measuring absorbance at $\lambda_{560\ nm}$ using a plate reader (SpectraMax M2, Molecular Devices).[98] Cells with reduced deformability have a higher probability of occluding pores and consequently exhibit a higher retention of fluid in the top well; we define the final volume of media retained in the top well compared to the initial volume loaded, $Vol_{final}/Vol_{initial}$, as % retention. While retention is not a direct readout for cell elastic modulus, we previously found that βAR activation increased the retention and stiffness of breast cancer cells as determined by atomic force microscopy (AFM).[15]

Real-time qPCR

Total RNA from lysates was extracted (Qiagen RNeasy Mini Kit), cleared of contaminating DNA with on-column DNase digestion (Qiagen RNase-Free DNase Set), and quantified by spectrophotometry (NanoDrop ND-1000; Thermo Scientific). Gene transcripts were examined by RT-qPCR with a CFX96 Touch Real-Time PCR Detection System (Bio-Rad), using one-step assay reagents (Qiagen Quantitect Probe RT-PCR) and TaqMan Gene Expression Assay primer-probes for human beta-2 adrenergic receptor, i.e., ADRB2 (Hs00240532_s1 from Thermo Fisher). Following reverse transcription of RNA template for 30 min at 50°C, resulting product underwent an initial activation step at 94°C for 15 min, followed by 50 amplification cycles of 15 s of strand separation at 94°C and 60 s of annealing and extension at 60°C. Triplicate determinations of each biological replicate were quantified by threshold cycle analysis of FAM fluorescence intensity using CFX Manager software (Bio-Rad), normalized to values of human GAPDH mRNA amplified in parallel (Hs02758991_g1).

Western blotting

Levels of proteins and protein phosphorylation were measured by western blotting. We loaded 30 μg of total protein into 4–12% Bolt gels (Invitrogen) with MES buffer (Invitrogen). Protein samples were transferred onto nitrocellulose membrane (GE Healthcare) with NuPAGE transfer buffer (Invitrogen). To minimize non-specific protein adsorption, we incubated membranes with blocking buffer (5% skim milk in TBS-T) at room temperature for 1 h. To quantify protein levels, we then incubated with the following antibodies: mouse anti-GAPDH (#MA5-15738, 1:5,000; ThermoFisher), rabbit anti-phospho-MLC2 (#3671 and #3674, 1:1,000; Cell Signaling), mouse anti-MLC2 (#4401, 1:1,000; Sigma), and mouse anti-RhoA (#MA1-134, 1:1,000; ThermoFisher). We measured the band density of the scanned film using ImageJ software (NIH, v1.50a).

Traction force microscopy – Pillars Assay

Micropillars were fabricated as previously described using PDMS and soft lithography.[99] To quantify pillar dimensions, we imaged the cross-section of the micropillar mold to determine the height of 6.5 ± 0.5 μm, and imaged the top view to determine the pillar diameter of 1.75 ± 0.5 μm. To facilitate darkfield imaging with a 20× objective (NA 0.5), gold micro-disks were bonded on the top of each pillar. Pillars were treated with 50 μg/mL fibronectin (Gemini Bio-Products). Prior to cell seeding, we imaged 5 regions of the pillar array. Cells were seeded and adhered overnight prior to treatment with drugs for 24 h. To delineate cells for traction force analysis, we stained cells with calcein AM (ThermoFisher) for 5 min at 37°C. The same 5 regions of the micropillar devices were then imaged using fluorescence microscopy (Zeiss Axiovert A1) equipped with a 20× objective (NA 0.5) to identify pillars occupied by cells. Darkfield microscopy was used to determine the positions of the gold-tipped pillars before and after cell seeding; displacements of the pillars that were caused by cells were determined using custom software (MATLAB). Source code is available at https://github.com/marvintan90/gaussianFittingForTraction.

The traction force, F, exerted by a cell on a single pillar was determined by:

$$F = \frac{4}{3}\pi E \frac{r^4}{L^3}\Delta x,$$

where E is the elastic modulus of the pillar (2.0 MPa), r is the radius of the pillar, L is the height of the pillar, and Δx is the horizontal displacement of the pillar between t_0 and $t_{measured}$.[99]

Traction force microscopy – Beads Assay

To quantify cellular traction force generation, we tracked the displacements of gold nanoparticles (diameter 400 nm) embedded in a polydimethylsiloxane (PDMS) substrate. Devices are fabricated as previously described.[100] In brief, we spin-coat a 75 μm-thick layer of PDMS onto a glass slide with a thickness of 150 μm; we then dispense gold nanoparticles suspended in citrate buffer (Sigma Aldrich 742090) onto the PDMS-coated glass slide and dry it in a vacuum desiccator (Thermo Scientific 53100250) overnight. Lastly, we spin-coat a top layer of PDMS (1:12.1 w/w, PDMS:hexane) with 300 nm thickness. To create a well on top of the traction membrane to contain cell medium, we place a PDMS ring on top of the layers: the ring is hole punched from a slab of pure PDMS 184 to have a 25mm outer diameter, 10mm inner diameter, and 3mm height. on top of the layers. Before each experiment, the PDMS surface inside the ring is coated with 50 μg/mL collagen in 1X PBS (Fisher, Corning 354236) for 1 h before 10,000 cells in 200 μL of DMEM are seeded and left to adhere overnight.

To collect traction force measurements, we image the cells in the device using a brightfield microscope (Zeiss Observer Z1) equipped with a 20× objective (NA 0.5). To quantify the effects of beta-adrenergic activation on cellular force generation, we treat cells with 100 nM isoproterenol or vehicle control, and image 2 h after treatment. Cells are then detached from the surface using 100 μL of 0.25% Trypsin-EDTA for 5 min. After cell detachment, we acquire a second set of brightfield images of the gold nanoparticles to serve as a reference image of the original bead positions. We then process the images through Zen (Zeiss) and Fiji/ImageJ to prepare them for quantitative image analysis for identifying single cells and tracking displacements of the gold nanoparticles in ImageJ/Fiji.

To calculate the traction force per cell, we developed an analysis suite based on methodology previously described by[101] that uses the displacement of beads over time to calculate the corresponding generated traction forces. In brief, we first isolate beads in the reference image and the cell-laden image by using image processing to allow the ImageJ particle analysis plugin to identify the beads as regions of interest. Next, we delineate the cell periphery by further image processing of the original brightfield image, thresholding the image by pixel value and density to isolate the plasma membrane, creating a ''cell edge mask.'' Then, we overlay this cell edge mask over the reference and cell-laden image, deleting beads that are outside of the mask and therefore outside of the cell edge. We want to select for beads on the cell edge and measure the displacements, as the majority of traction stresses exist on cell periphery. Using ImageJ's PIV and FTCC plugins, we are given the stress in Pascals calculated from the bead displacement, which is then converted to nanonewtons. We then average by the number of beads used to generate the traction force for each cell to account for the variation in number of beads that may be on the cell edge between different cells. The final metric per single cell is the traction force generated and averaged by the number of beads on the periphery of the cell.

Three-dimensional (3D) scratch wound invasion assay

To measure the invasion of cells through a 3D matrix, we used a 3D scratch wound assay.[15,57] A 96-well plate (ImageLock, Essen BioScience) was pre-coated with 100 μg/mL Matrigel (Corning). We then plated 3×10^4 cells transfected with siRhoA or siControl

(at post-transfection 24 h) into each well and incubated for 48 h. We generated 700–800 μm wide wounds in near 100% confluent cell monolayers using a 96-pin mechanical device (WoundMaker, Essen BioScience). Cells were then washed with DMEM medium and 8 mg/mL Matrigel was added to cover the entire well. After a 30 m incubation at 37°C to solidify the Matrigel, 100 μL of culture medium containing isoproterenol and/or propranolol was added. We acquired images every 2 h and determined the relative wound density and cell confluency using IncuCyte software (Essen BioScience). Relative wound density is defined as the area of cells in the newly healed scratch wound region (purple) compared to the area of the initial scratch wound (teal at time 0 h). To determine any differences in proliferation rates, which can also impact wound healing rates, we measured the proliferation of cells on Matrigel (Figures S1B and S1C).

Viability and apoptosis assays

Cell viability after drug treatment was determined by measuring the number of live, dead, and apoptotic cells using the Dead Cell Apoptosis Kit (ThermoFisher). MDA-MB-231^{HM} cells were cultured and treated with kinase inhibitors (Y27632, g-H-1152, ML-7, IPA-3) and βAR-modulating drugs (isoproterenol, propranolol). Blebbistatin and Paclitaxel were used as positive controls for inhibtion of myosin and induction of apoptosis, respectively. As a positive control for the apoptosis assay, 5×10^5 cells were treated with paclitaxel (1, 10, and 100 μM) for 24 h. After drug treatment, culture media was collected to harvest dead floating cells; adherent cells were washed with Phosphate-Buffered Saline (PBS) prior to trypsinization. After spindown of the suspension of trypsinized and dead cells at 1,500 rpm for 3 min, cell pellets were resuspended and stained with recombinant annexin V conjugated to fluorescein (Alexa Fluor 488 annexin V) and propidium iodide (PI) as per the manufacturer's protocol. Populations of live (annexin V negative, PI negative), dead (PI positive), and apoptotic (annexin V positive, PI negative) cells were analyzed by flow cytometry (LSRII, BD Biosciences).

RNA-seq analysis

To quantify expression levels of *ADRB2* and genes in the RhoA-ROCK-NMII axis across MDA-MB-231, MCF7, and MCF10A cell lines, we used publicly available RNA-Seq data[S1]. Raw fastq files were trimmed based on quality score and N calling reads. For the quality score trimming, we trimmed reads showing poor quality scores (<20) from both 5′-end 10bp and 3′-end 50bp windows. For the N calling read trimming, we trimmed reads containing Ns at 3′-end 15bp window. We also filtered out short trimmed reads (<30 bp) and reads with poor average quality scores (<21) or low read accuracy values (<−1). Read accuracy value describes the probability that a read is accurate and was calculated from quality score following the below formula:

$$\textit{Read accuracy value} = \sum_{n=1}^{k} log_2\left(1 - 10^{-\frac{quality\ score_n}{10}}\right)$$

The reads were further trimmed to remove the contamination of adopters and polyA signals using cutadapt (version 1.14)[S2]. The sequence qualities of fastq reads were tested before and after the trimming process using both FastQC (version 0.11.8)[S3] and FastQ Screen (version 0.13.0)[S4]. After read trimming, we downloaded hg38 reference genome (GENCODE v32). We considered only chromosomes without contigs and prepared STAR index using its matched gtf file (gencode.v32.annotation.gtf.gz). The trimmed reads were aligned to the index using SRAR (version 2.5.3a)[S5] following parameters:

STAR –runMode alignReads –alignSJoverhangMin 10 –alignSJDBoverhangMin 1 –alignIntronMax 1000000 –outFilterMultimapNmax 10 –outFilterMismatchNmax 3.

From uniquely mapped reads, we counted reads from each gene containing transcripts (≧ 200bp) as considering alignment directions using featureCounts (version 1.6.0)[S6] following:

featureCounts -s 2 -O -t exon -g gene_id

From read counts showing forward direction to transcripts, we calculated Reads Per Kilobase of transcript per Million mapped reads (RPKM) values after adding one more count (read count +1)[S7].

Computational modeling

To study the increase in cell traction forces as a consequence of increased diphosphorylated-MLC2 (ppMLC2), we employed a stochastic model of actin-myosin force generation[44] coupled with actin-integrin-substrate adhesion dynamics (as detailed in STAR Methods) (Figures 3A and S6). In summary, the model simulates individual myosin motors transitioning between activate and inactive states, the cycling of active myosin through the cross-bridge cycle,[102–104] force generation and actin filament sliding due to myosin binding and conformational change, and force transmission between sliding actin filaments and substrate via reversible integrin-surface catch bonds. Integrating the force transmitted by a fixed number of actin filaments to the substrate within a 1 μm^2 area gives the traction stresses generated by the cells. In this model, focal adhesions were modeled as multiple actin filaments ($\sim$120/μm^2)[105–107] tugging on substrate bound integrins by the action of myosin motors ($\sim$60/actin filament).[108–111] Individual actin-myosin filament interactions as well as integrin dynamics were simulated using a stochastic Monte Carlo approach.[112] The activity of each individual motor is regulated by its phosphorylation state, ATP binding and hydrolysis rates, as well as the pushing or pulling forces acting on each motor (Figure 3A). We used the experimentally determined ratio of ppMLC2/MLC2 (Figure 1D) as an input to the model to capture ROCK-dependent MLC2 phosphorylation and dephosphorylation rates. We assume that myosins with dephosphorylated light chains are incapable of interacting with actin filaments, as these myosins assemble in compact states with the ATPase activity of the

myosin heads being blocked.[39] When the MLC is phosphorylated, the myosin is available to interact with the actin filament. The myosin head binds to a specific binding site on a neighboring actin filament upon the hydrolysis of ATP. The release of the phosphate group is force dependent, where a pushing or pulling of the bound myosin head by fluctuations in the actin filament from binding, force generation and unbinding of neighboring myosins can alter the reaction rates.[47] The release of ADP is a relatively faster process and is assumed to be unaffected by the same forces.[113] Upon release of ADP, the myosin binds to an ATP molecule releasing the actin filament in a force dependent manner and goes back to the active unbound state where it started from when phosphorylated from where it can either re-enter the cross-bridge cycle or become inactive due to dephosphorylation. These states are described in Figure 3A. The model is used to predict the change in traction forces as a function of rate of myosin activation and deactivation associated with MLC2 phosphorylation and dephosphorylation. The model is also used to predict the change in traction forces as a function of substrate stiffness as substrate stiffness affects the rate at which force is generate within the actin-myosin filaments and consequently the dissociation dynamics of the cell-substrate adhesions.[44]

To predict cellular traction forces, we use a simplified version of the model, which is described in our previous work[S8]. We limit the model here to focus on individual actin-myosin filaments interacting with integrin-based adhesions without the effect of actin branching or force dependent recruitment of additional actin-myosin filaments, as our previous work did not show significant impact of these processes within the timescales relevant to the model. We assumed that traction forces are generated by actin myosin filaments that are attached to surface bound integrin receptors[S9–11] and calculated traction stresses using a density of 120 actin filaments per μm^2 based on experimental observations[S12,13]. For the sake of simplicity, we also assumed the force generation, attachment, and detachment of individual actin filaments to be independent of each other. The force generation in each actin filament was calculated using a modified version of the myosin crossbridge cycling model[S14–16]. Input values for the model are obtained from our experimental data and the literature wherever possible (Table S1).

Our approach is based on existing force generation models that assume a half-sarcomere-like structure within which myosins cycle through various states of ATP binding and hydrolysis, as well as corresponding actin-myosin binding, conformational changes, and detachment[S17–19]. In our model[S20], each myosin cycles through 5 states (Figure 3A). The inactive state (state 15) is the dephosphorylated state, from which it transitions reversibly to a phosphorylated active state (state 2)[S21]. In state 2, the myosin has a bound ATP molecule. Upon ATP hydrolysis, the myosin binds reversibly to a neighboring binding site on the actin filament (state 3); this binding may result in a strain in the myosin stalk. Upon release of the phosphate group, the myosin undergoes an irreversible, force-generating conformational change (state 4). Upon ADP release, the myosin remains bound to the actin filament (state 1). As another molecule of ATP binds to the myosin head, the myosin releases from actin and is available for another cycle of force generation (state 2). The transition rates between the any two states i and j are labeled as k_{ij} (Table S1). The ratio of transition rates between the dephosphorylated (state 15) and phosphorylated (state 2) myosin states was derived from the experimental ratios of ppMLC2:MLC2 obtained from western blots (Figure 1D) using a steady state relationship between rates and concentrations,

$$\frac{k_{152}}{k_{215}} = \frac{ppMLC2}{MLC2}. \quad \text{(Equation 1)}$$

Transition rates in the bound motor states 3 and 1 are modified by strain in the motor tails due to the forces acting on the tail or stalk[S19], the effect of which is modeled as

$$ks_{12} = k_{12}\, exp\left(\frac{\frac{1}{2}k_m\epsilon^2}{k_BT}\right) \quad \text{(Equation 2)}$$

and

$$ks_{34} = k_{34}\, exp\left(\frac{k_m\epsilon\delta}{k_BT}\right), \quad \text{(Equation 3)}$$

where k_m is the stiffness of the motor stalk, ϵ is the strain in the stalk, k_B is the Boltzmann constant, T is the absolute temperature, and δ is the distance between myosin binding sites. Once the different myosin states are determined and the transition rates quantified, the state transition ordinary differential equations can be either numerically solved or the transition of each myosin through the various states can be simulated using a stochastic Monte Carlo simulation to iteratively track the strain in the stalk of each individual myosin and calculate the strain-dependent transition rates. We simulate 60 myosin motors per actin filament[S22]. We consider a small time step of 1 ms in which we update the states of each of the myosin motors within an individual filament with a probability given by Equation 4,

$$P_{ij}(t < \Delta t) = 1 - exp\ \ exp\left(-ks_{ij}\Delta t\right). \quad \text{(Equation 4)}$$

We assume that within the small time step Δt, the transition rates are constant. At any given point in time, the forces generated within the actin filament due to actin-myosin interactions are computed using Equation 5,

$$F_{act}(t) = (k_m N_4(t) y) - \left(k_m \sum N_{1,3,4}\epsilon\right), \quad \text{(Equation 5)}$$

where N_i is the number of motors in state i and y is the motor step size. The first term represents the active force generated by the motors and the second term represents the passive force on the actin filament by strain in the stalks of attached motors. The myosin-generated force on actin filaments is transferred to integrins at the focal adhesion/ECM interface. The displacement, x, of the actin filament pulling against the substrate is given by solution of

$$F_{act} - k_{spring}x = \gamma \frac{dx}{dt}, \quad \text{(Equation 6)}$$

where k_{spring} is the effective spring constant of the substrate and the integrin protein, and γ is drag on the actin filament[S23].

The integrin catch-slip bond dissociation rate k_{cs} is modeled by

$$k_{cs} = \frac{1}{k^0_{catch}Aexp\left(\frac{-f\varepsilon}{k_BT}\right)+\left(k^0_{slip}Bexp\left(\frac{f\varepsilon}{k_BT}\right)+Cexp\left(\frac{-f\varepsilon}{k_BT}\right)\right)^{-1}}, \quad \text{(Equation 7)}$$

where k_{catch} represents the catch regime, k_{slip} is the slip regime, ε is the energy length scale for binding/unbinding[S24], and $f\ (=k_{spring}x)$ is the force experienced by the integrin bond[S25]. Within a certain force range, integrin bond lifetimes increase, however, the bond will revert to a slip bond if the force exceeds the range. The binding and unbinding transition probabilities of actin filament-bound integrins with the substrate are calculated using Equation 4, where i and j are now the bound and unbound states.

Traction forces at time (t) are calculated as the net force transmitted from all the actin filaments to the substrate via attached integrin bonds as shown in Equation 8.

$$F_{tract} = \sum f_i H_i \begin{cases} H_i = 1 \text{ if SF - integrin complex is attached to the substrate, else} \\ H_i = 0 \end{cases}, \quad \text{(Equation 8)}$$

where f_i is the force generated at each actin-integrin-substrate bond.

Source code is available at https://github.com/compactmatterlab/bAR-forces/tree/master/bAR-forces.

QUANTIFICATION AND STATISTICAL ANALYSIS

Statistical analyses

All experiments were performed at least three independent times, unless otherwise stated. Statistical significance between control and treated groups was determined with Mann Whitney non-parametric testing or one-way ANOVA with Tukey's multiple comparison post hoc analysis using GraphPad Prism 8 (GraphPad Software, La Jolla, CA). For the traction force data from the bead assay, which is non-normally distributed and has smaller sample sizes, we use permutation testing. P-values are determined by comparing the distribution of medians generated by resampling our data for 5000 iterations per cell line. Error bars for data from the computational model represent the standard error of the mean of over >20 samples. Each sample is a 1 s long simulation of myosin generated traction forces in 120 actin filaments.